Structural basis of LRPPRC-SLIRP-dependent translation by the mitoribosome

Vivek Singh[1,7], J. Conor Moran[2,7], Yuzuru Itoh[1,6,*], Iliana C. Soto[3], Flavia Fontanesi[2], Mary Couvillion[3], Martijn A. Huynen[4], Stirling Churchman[3,*], Antoni Barrientos[5,*], Alexey Amunts[1,*]

[1] Science for Life Laboratory, Department of Biochemistry and Biophysics, Stockholm University, Solna 17165, Sweden.

[2] Department of Biochemistry and Molecular Biology, University of Miami Miller School of Medicine, Miami FL 33136, USA

[3] Blavatnik Institute, Department of Genetics, Harvard Medical School, Boston MA 02115, USA.

[4] Medical BioSciences, Radboud University Medical Center, Nijmegen 6525, the Netherlands.

[5] Department of Neurology, University of Miami Miller School of Medicine, Miami FL 33136, USA.

[6] Current address: Department of Biological Sciences, Graduate School of Science, University of Tokyo, 113-0033 Tokyo, Japan.

[7] These authors contributed equally

* correspondence: yuzuru.itoh@bs.s.u-tokyo.ac.jp, churchman@genetics.med.harvard.edu, abarrientos@med.miami.edu, amunts@scilifelab.se

In mammalian mitochondria, mRNAs are co-transcriptionally stabilized by the protein factor LRPPRC. Here, we characterize LRPPRC as an mRNA delivery factor and report its cryo-EM structure in complex with SLIRP, mRNA and the mitoribosome. The structure shows that LRPPRC associates with the mitoribosomal proteins mS39 and the N-terminus of mS31 through recognition of the LRPPRC helical repeats. Together, the proteins form a corridor for hand-off the mRNA. The mRNA is directly bound to SLIRP, which also has a stabilizing function for LRPPRC. To delineate the effect of LRPPRC on individual mitochondrial transcripts, we used an RNAseq approach, metabolic labeling and mitoribosome profiling that showed a major influence on ND1, ND2, ATP6, COX1, COX2, and COX3 mRNA translation efficiency. Our data suggest that LRPPRC-SLIRP acts in recruitment of mitochondrial mRNAs to modulate their translation. Collectively, the data define LRPPRC-SLIRP as a regulator of the mitochondrial gene expression system.

The mitoribosome is organised in a small and large subunit (SSU and LSU) that are assembled from multiple components in a coordinated manner and through regulated sequential mechanisms [1-5]. The SSU formation is accomplished by the association of the mitoribosomal protein mS37 and the initiation factor mtIF3, leading to a mature state that is ready for translation of the mRNA [3,6]. In mammals, mitochondrial transcription is polycistronic and gives rise to two long transcripts, corresponding to almost the entire heavy and light mtDNA strands. The individual mRNAs are available for translation only after they are liberated from the original polycistronic transcripts and polyadenylated [7]. In *Escherichia coli*, a functional transcription-translation coupling mechanism has been characterised involving a physical association of the RNA polymerase with the SSU, termed the expressome [8-10]. In contrast, in mammalian mitochondria, nucleoids are not compartmented with protein synthesis; mitoribosomes are independently tethered to the membrane [11,12], and no coupling with the RNA polymerase has been reported. In addition, human mitochondrial mRNAs and the mitoribosome do not have the Shine–Dalgarno (SD) and anti-SD sequences that are used to recruit mRNA to SSU in bacteria [13]. Mitochondrial mRNAs also lack cap 5′ modifications, which is a hallmark of eukaryotic cytosolic mRNAs translation initiation. In the cytosol, mRNA is recruited to a pre-initiation complex, consisting of the SSU and translation initiation factors, which then scans along the 5′ untranslated region to find the start codon [14,15]. No equivalent mechanism has been found in

61 mitochondria, and thus, how mRNAs are delivered for translation in mitochondria remained
62 unknown.

63 The 130-kDa protein factor LRPPRC (leucine-rich pentatricopeptide repeat-containing protein),
64 a member of a Metazoa-specific pentatricopeptide repeat family, was reported to act as a global
65 mitochondrial mRNA chaperone that binds co-transcriptionally [16-18]. LRPPRC is an integral part
66 of the post-transcriptional processing machinery required for mRNA stability, polyadenylation,
67 and translation [16-19]. Mutations in the gene encoding for LRPPRC lead to French-Canadian type
68 Leigh syndrome (LSFC) an untreatable paediatric neurodegenerative disorder caused by
69 ultimately impaired mitochondrial energy conversion [20].

70 LRPPRC has been reported to interact with a small 11-kDa protein cofactor SLIRP (SRA stem-
71 loop-interacting RNA-binding protein) [21,22] that plays roles in LRPPRC stability and maintaining
72 steady-state mRNA levels [23]. *SLIRP* silencing results in the destabilization of respiratory
73 complexes, loss of enzymatic activity, and reduction in mRNA levels, implicating a role in
74 mRNA homeostasis [24]. *SLIRP* variants cause a respiratory deficiency that leads to mitochondrial
75 encephalomyopathy [25]. In addition, *SLIRP* knockdown results in increased turnover of LRPPRC
76 [23,25,26], and *in vivo* co-stabilisation suggests that the two entities have interdependent functions
77 [23,27]. The interaction of LRPPRC and SLIRP *in vitro* has been previously studied [28].

78 LRPPRC has also been implicated in coordinating mitochondrial mRNA stability and translation
79 [18,29]. Previous analysis showed a correlation between presence of LRPPRC and mRNA on the
80 mitoribosome [30]. However, there are no structures available for LRPPRC, SLIRP, or any
81 complexes containing them, and *in vitro* reconstitution could not provide meaningful
82 information, in part because not all the components of the mitochondrial gene expression system
83 have been characterised. Thus, although isolated mitoribosomal models have been determined [31-
84 33], the molecular mechanisms of mRNA delivery to the SSU for activation of translation and the
85 potential involvement of LRPPRC-SLIRP in this process remained unknown.

86

87 **Results**

88 **Structure determination of LRPPRC-SLIRP bound to the mitoribosome**

89 To explore the molecular basis for translation activation in human mitochondria, we used low
90 salt conditions to isolate a mitoribosome:LRPPRC-SLIRP-mRNA complex for cryo-EM. We

91 merged particles containing tRNAs in the A- or P-site, as well as an extra density in the vicinity
92 of the mRNA entry channel and applied iterative local-masked refinement and classification with
93 signal subtraction (Extended Data Fig. 1a). It resulted in a 2.9 Å resolution map of the
94 mitoribosome during mRNA delivery to the SSU, with the local resolution for the LRPPRC
95 binding region of ~3.4 Å (Extended Data Fig. 1b,c). The reconstruction showed a clear density
96 only for the LRPPRC N-terminal domains (residues 64-644, average local resolution ~4.5 Å)
97 bound to the SSU head, which is consistent with a previous mass-spectrometry analysis
98 (Extended Data Fig. 1d,e) [30]. It allowed us to model 34 α-helices, 17 of which (α2-18) form a
99 ring-like architecture, while the rest form an extended tail that adopts a 90° curvature and
100 projects 110 Å from the SSU body in parallel to the L7/L12 stalk (Fig. 1a,b). The C-terminal
101 domains (residues 645-1394) were not resolved. The complete LRPPRC model obtained with
102 *AlphaFold2* [34] combined with Translation/Liberation/Screw Motion Determination (TLSMD)
103 analysis [35,36] defined the C-terminal domains as individual segments, indicating potential
104 flexibility (Extended Data Fig. 2).

105 When LRPPRC-SLIRP is bound to the mitoribosome, a previously disordered density of mS31
106 that extends from the core also becomes ordered, revealing its N-terminal region (Fig. 2a). This
107 region is arranged in two helix-turn-helix motifs, offering a 1930 $Å^2$ surface area for direct
108 interactions with LRPPRC (Fig. 1c, Fig. 2). The position of the LRPPRC residue 354, in which
109 the mutation A354V leads to LSFC with a clinically distinct cytochrome *c* oxidase deficiency
110 and acute fatal acidotic crises is in a buried area of helix 17, close to the mRNA binding region
111 (Fig. 1c, Extended Data Fig. 2a). A previous study demonstrated that the mutation is
112 abolishing the interaction with the protein SLIRP [37]. Consistent with mass spectrometry analysis
113 [28] and the interaction interface previously determined [37], the remaining associated density was
114 assigned as SLIRP, found to be located close to the Epsin N-terminal homology (ENTH) domain
115 of LRPPRC (Fig. 2a). Finally, SLIRP is connected to an elongated density on the LRPPRC
116 surface that is also associated with six of the mitoribosomal proteins and corresponds to the
117 endogenous mRNA (Fig. 2).

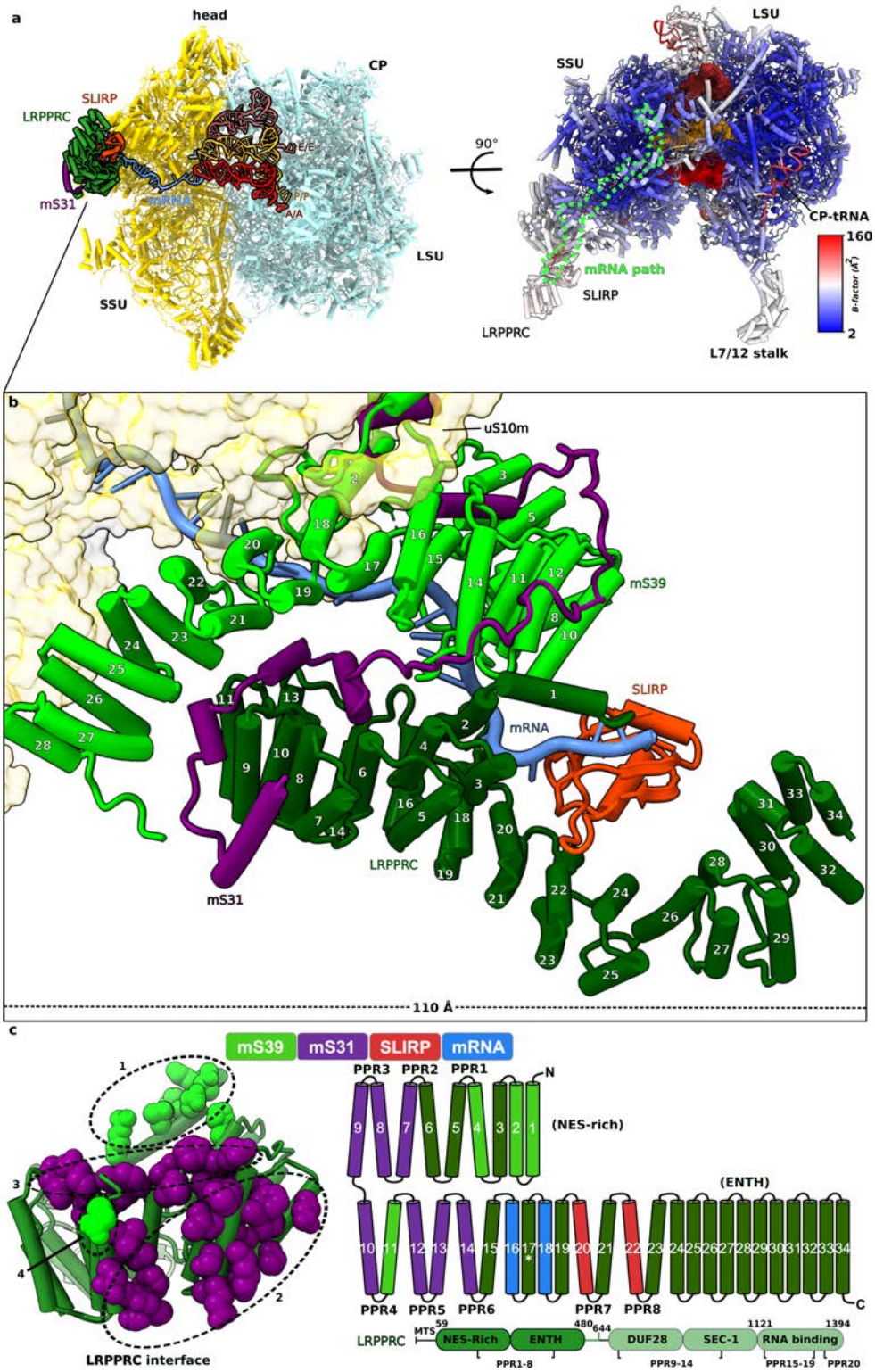

Figure 1. Structure of mitoribosome with LRPPRC-SLIRP bound to mRNA.
a, Overview of the mitoribosome:LRPPRC-SLIRP model. Right panel, top view of the model colored by atomic *B*-factor (Å^2), tRNAs in surface (red, orange, brown), mRNA path (light green) is highlighted. **b,** A close-up view of the mitoribosome:LRPPRC-SLIRP-mRNA

interactions. LRPPRC associates with mS31-m39 via a ring-like structure (α2-18) that together form a corridor for the hand-off the mRNA from SLIRP. **c,** Contact sites between LRPPRC and mS31-mS39 (within 4 Å distance), view from the interface. Right panel, schematic diagram showing the topology of LRPPRC consisting of 34 helices. Colours represent engagement in interactions with mS39 (light green), mS31 (purple), SLIRP (orange), mRNA (blue). The position of LSFC variant (A354V) is indicated with an asterisk on helix 17.

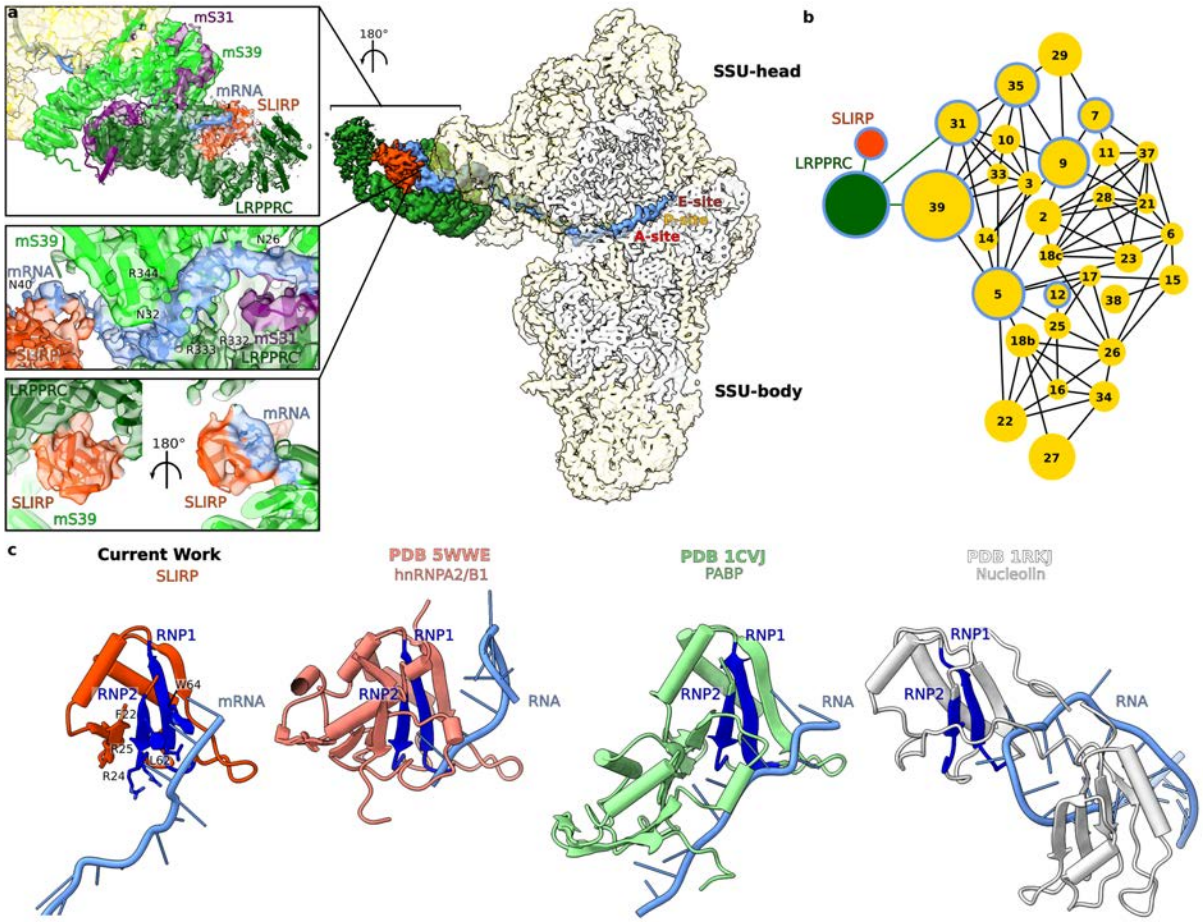

Figure 2. Overview of density for LRPPRC, SLIRP and mRNA and their interactions with SSU proteins.

a, The density map for LRPPRC (dark green), SLIRP (orange), mRNA (blue) on the SSU is shown in the centre. The model and map for mS39-LRPPRC-SLIRP and corresponding bound mRNA residues are shown in closeup views on the left, and arginines involved in mRNA binding are indicated. The bottom closeup views show SLIRP with its associated densities for LRPPRC and mRNA. For clarity, the map for SLIRP has been low-pass filtered to 6 Å resolution. **b,** Schematic of protein-protein interactions, where node size corresponds to relative molecular mass. Nodes of proteins involved in mRNA binding are encircled in blue. **c,** RRM containing proteins: SLIRP, hnRNPA1/B2 (PDBID 5WWE), PolyA binding protein (PABP, PDBID 1CVJ) and Nucleolin (PDBID 1RKJ) are shown in complex with RNA with RNP1 and RNP2 sub-motifs colored blue.

142 **SLIRP is stably associated with mRNA and LRPPRC on the SSU**

143 The binding of SLIRP in our model is enabled via LRPPRC helices α20 and 22, which is
144 consistent with crosslinking mass spectrometry data and mutational analysis [28]. The structure
145 reveals that SLIRP links the nuclear export signal (NES) domain with the curved region of the
146 ENTH domain of LRPPRC (Fig. 1b, Fig. 1c). This binding of SLIRP contributes to a corridor for
147 the mRNA that extends to mS31 and mS39 (Fig. 1b, Supplementary Video 1). Through this
148 corridor, the mRNA extends over ~180 Å all the way to the decoding center (Fig. 2a). In our
149 structure, SLIRP is oriented such that the conserved RNA recognition motif (RRM), including its
150 submotifs RNP1 (residues 21-26) and RNP2 (residues 60-67) [38-40] form an interface with
151 modeled mRNA (Fig. 2). The arrangement of RNP1 and RNP2 with respect to the mRNA is
152 similar to that observed in previously reported structures of other RRM proteins [41-43] (Fig. 2c,
153 Extended Data Fig. 3). Moreover, residues R24, R25 of RNP2 and L62 of RNP1 motifs
154 previously implicated to be required for RNA binding by SLIRP [37] are positioned within an
155 interacting distance of the mRNA (Fig. 2a). Thus, SLIRP contributes to the LRPPRC specific
156 scaffold, and accounts for a role in binding the mRNA.

157 The *B*-factor distribution of SLIRP in our model is similar to that of LRPPRC, while still lower
158 than some of the more mobile components of the mitoribosome, such as the acceptor arm of the
159 CP-tRNA^{Val} (Fig. 1a). This indicates a functionally relevant association with LRPPRC in terms
160 of stability of binding. Our finding that SLIRP is involved in hand-off the mRNA to the
161 mitoribosome provides a mechanistic explanation for the previous results from biochemical
162 studies showing that SLIRP affects LRPPRC properties *in vitro* [27,28], and the presentation of the
163 mRNA to the mitoribosome *in vivo* [23].

164 Since in *E. coli*, the expressome-mediating protein NusG was proposed to regulate mRNA
165 unwinding [8], and SSU proteins uS3 and uS4 have an intrinsic RNA helicase activity [44], we
166 searched for known helicase signature motifs [45] in the LRPPRC sequence, but no such motifs
167 were present. In the mitoribosome, where the mRNA channel entry site is located, a bacteria-like
168 ring-shaped entrance is missing, the entrance itself has shifted, and its diameter expanded [31]. The
169 mRNA extends all the way into the head/beak of the SSU stabilised by mitoribosome-specific
170 components: mS39 helical repeats, mS35 N-terminus that extends from the side of the SSU head,
171 and N-terminal extension of uS9m that contacts the mRNA nucleotide at position 15 (numbered
172 from the E-site).

173 **LRPPRC-SLIRP hands-off the mRNA to mS31-mS39, channeling it for translation**

174 Next, we analysed the structural basis for the complex formation. The association of LRPPRC
175 with the mitoribosome involves the helices α1, 2, 6-11, that form a mitoribosome-binding
176 surface (Fig. 1b, Fig. 1c). The binding is mediated by four distinct contacting regions (Extended
177 Data Fig. 6): 1) α1-2 (residues 64-95) is flanked by a region of mS39, a PPR domain-containing
178 protein, that consists of four bundled helices (α11-14); 2) α7 and 9 form a shared bundle with
179 two N-terminal helices of mS31 (residues 175-208, stabilized by C-terminal region of mS39) that
180 encircle the NES-rich domain to complement the PPR domain; 3) α10-11 are capped by a
181 pronounced turn of mS31 (residues 209-232) acting as a lid that marks the LRPPRC boundary,
182 and it is sandwiched by the mS39 helix α19 and C-terminus from the opposite side; 4) in
183 addition, α11 is also positioned directly against the helix α23 of mS39. Thus, LRPPRC docks
184 onto the surface of the mitoribosome via mS31-mS39, which are tightly associated with each
185 other, and each provides two contact patches to contribute to stable binding.

186 Based on the structural analysis, the hand-off of the mRNA for translation is mediated by four of
187 the LRPPRC helices: α1, 2, 16, and 18 (Fig. 1b, Fig. 1c, Supplementary Video 1). The mRNA
188 nucleotides 33-35 (numbered from the E-site) are stabilized in a cleft formed by α1-2 on one side
189 and α16, 18 on the other. Nucleotides 31 and 32 contact residues R332, R333 from LRPPRC, as
190 well as R344 from mS39 (Fig. 2a). This region is within 120-130 Å from the P-site. The
191 involvement of the NES-rich domain of LRPPRC in mRNA binding in our structure is consistent
192 with a biochemical analysis of recombinant LRPPRC where the N-terminal PPR segments were
193 systematically removed, which showed a reduced formation of protein-RNA complexes [28]. The
194 rest of the mRNA is situated too far from LRPPRC to interact with it. Here, the mRNA is handed
195 to mS31-mS39, consistently with a translation initiation complex [46].

196 In the structure, mS31, mS39, and LRPPRC together form a 60-Å long corridor that channels the
197 mRNA from SLIRP toward the mitoribosomal core (Fig. 1b, Supplementary Video 1). The
198 binding of LRPPRC is mediated by four distinct contact regions (Extended Data Fig. 6): contact-
199 1 is formed by α1-2 (residues 64-95) flanked by the mS39 PPR domain of four bundled helices
200 (α11-14); contact-2 is formed by α7, 9 that generate a shared bundle with two N-terminal helices
201 of mS31 (residues 175-208, stabilized by C-terminal region of mS39) that encircle the head to
202 complement the PPR domain; contact-3 is formed by α10-11 that are capped by a pronounced
203 turn of mS31 (residues 209-232) acting as a lid that marks the LRPPRC boundary, and it is

204 sandwiched by the mS39 helix α21 and C-terminus from the opposite side; contact-4 is formed
205 by α11 that is positioned directly against the mS39 α23.

206 With respect to mRNA binding, nucleotides 26-30 bind mS39 PPR domain 5, and nucleotide 26
207 connects to contact-2 (Fig. 2a, Extended Data Fig. 6). Thus, the mRNA hand-off is achieved
208 through functional cooperation between LRPPRC-SLIRP and mS31-mS39. Therefore, in the
209 mitoribosome:LRPPRC-SLIRP with mRNA model, LRPPRC performs three functions:
210 coordination of SLIRP, which plays a key role in the process of mRNA recruitment, association
211 with the SSU, and hand-off of the mRNA for translation (Fig. 1, Extended Data Fig. 6).
212 Supplementary Video 1).

213

214 **LRPPRC is recruited for translation of mRNAs**

215 Next, we asked whether LRPRRC-SLIRP delivers all mRNAs to the mitoribosome or is
216 selective. We generated an *LRPPRC*-knockout cell line [29] that was rescued with either a wild-
217 type *LRPPRC* or a variant carrying the LSFC founder mutation A354V [20] (Extended Data Fig.
218 4). The steady-state levels of the LSFC variant were reduced by 60%, suggesting protein
219 instability as reported in patients [22], and the levels of SLIRP were equally decreased (Extended
220 Data Fig. 4). We then implemented an RNAseq approach that confirmed a substantially depleted
221 mitochondrial transcriptome [17,47,48] (Fig. 3a). In the LRPPRC-knockout, transcripts from the
222 heavy strand were lowered by 1.5-4-fold, except for ND3, which remained stable, consistent
223 with protein synthesis data (Fig. 3b), while the single light strand-encoded *ND6* mRNA was not
224 affected as reported [16], and the effect of the LSFC mutation on RNA stability was limited to six
225 transcripts (Fig. 3a), indicating LRPPRC's role in heavy strand mRNA stability is non-specific.
226 Metabolic labeling assays using [^{35}S]- methionine indicated that incorporation of the
227 radiolabeled amino acid into most newly synthesized mitochondrial proteins is severely
228 decreased in *LRPPRC*-KO cells (Fig. 3b). However, there were differential effects among
229 transcripts; synthesis of ND3, ND4L, and ATP8 remained above 50% of the WT, but translation
230 of other transcripts proceeded at a lower rate (*e.g.*, *ND1*, *ND2*, or *ATP6*) or was virtually blocked
231 (*e.g.*, *COX1, COX2, or COX3)* (Fig. 3b). The translational defect results in a decrease in the
232 steady-state levels of the four OXPHOS complexes that contain mtDNA-encoded subunits
233 (Extended Data Fig. 5).

234 To assess whether the mitochondrial translation efficiency (TE) is decreased in an mRNA-
235 specific manner in the *LRPPRC*-knockout, we performed mitoribosome profiling (Fig. 4). These
236 data show a decreased TE, calculated by dividing spike-in normalized ribosome footprint reads
237 by the spike-in normalized RNA sequencing reads (in other words, how well a particular
238 transcript is translated) [49,50]. In *LRPPRC*-knockout cells, TE was attenuated for *COX1* and *COX2*
239 transcripts and the bicistronic *ATP8/ATP6* transcript, intriguingly more for ATP6 than ATP8
240 (Fig. 4a). Thus, our data suggest that LRPPRC-SLIRP is required for the translation of some
241 transcripts, in agreement with the metabolic labeling of newly synthesized mitochondrial
242 products (Fig. 3b).

243 To support the role of LRPPRC in mRNA binding, we determined an average length of the
244 mitoribosome-protected fragments using mitoribosome profiling (Fig 4b). In the *LRPPRC*-
245 knockout cells, we observed a decrease in the average protected fragment length, compared to
246 the wild type (Fig 4b). This observation is consistent with the structural data showing the
247 association of LRPPRC with mRNA and the mitoribosome. Previous studies also showed that
248 LRPPRC–SLIRP relaxes structures of mRNAs [17], potentially to expose it to initiate translation
249 [16]. The average protected fragment length in LSFC cells were smaller than in wild-type cells,
250 similar to the *LRPPRC*-knockout (Fig 4b), suggesting that whereas the mutant protein
251 participates in translation, it does so differently than the wild-type protein

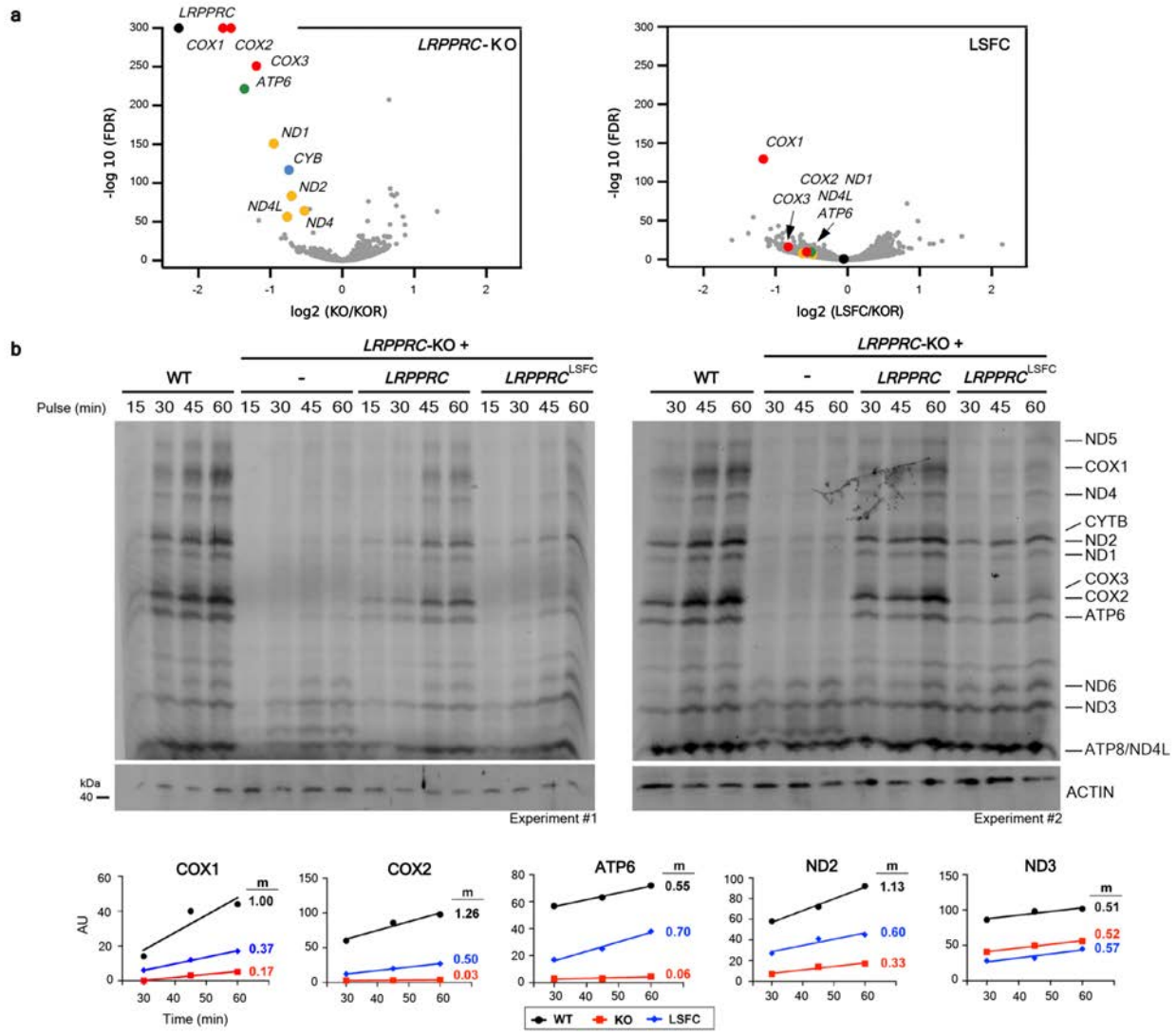

Figure 3. Mechanism of LRPPRC-SLIRP mediated mRNA binding and stabilization. **a,** Whole-cell RNAseq normalized by read depth, comparing *LRPPRC*-KO cells (KO) with KO cells reconstituted with WT *LRPPRC* (KOR) or the LSFC variant (A354V). The results are the average of two biological replicates. The differentially expressed mitochondrial transcripts are color-coded: coding for subunits of cytochrome *c* oxidase (CIV) in red, NADH dehydrogenase (CI) in yellow, coenzyme Q-cytochrome *c* oxidoreductase (CIII) in blue, and ATP synthase (CV) in green. **b,** Metabolic labeling with [^{35}S]-labeled methionine of newly-synthesized mitochondrial polypeptides for the indicated times, in the presence of emetine to inhibit cytosolic protein synthesis, in whole HEK-293T WT, *LRPPRC*-KO cells, and KO cells reconstituted with LRPPRC (KO+WT) or the LSFC variant (KO+LSFC). Bottom panel, representative plots of [^{35}S]-labeled methionine incorporation into specific polypeptides in WT or *LRPPRC*-KO cells. The images were quantified in two independent experiments.

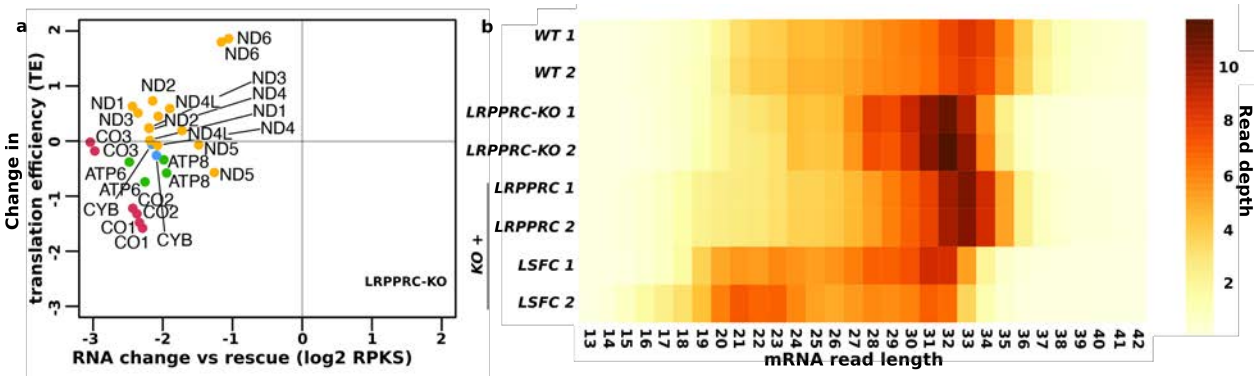

Figure 4. Mitochondrial translation efficiency is decreased in *LRPPRC*-KO cells. a, Change in TE and RNA abundance in *LRPPRC*-KO cells compared to LRPPRC-reconstituted cells ("rescue"). Mitoribosome profiling data and RNA-seq data were normalized using a mouse lysate spike-in control (RPKS) [29], then TE was calculated from these normalized values (mitoribosome profiling / RNA-seq). Biological replicates are shown as individual points. The mitochondrial transcripts are color-coded as in Fig. 3. **b**, Heat map showing the length distribution for reads mapping to mitochondrial mRNAs [29].

The mitoribosome:LRPPRC-SLIRP complex is specific to Metazoa

To place the structural data into an evolutionary context, we performed comparative phylogenetic analysis of the proteins involved in the mRNA hand-off process. Since the mitochondrial rRNA has been generally reduced in Metazoa [51], we examined whether this loss might coincide with the origin of LRPPRC and its interactors. The orthology database EGGNOGG [52] and previous analysis [53] indicated that LRPPRC and mS31 are only present in Bilateria, while mS39 only occurs in Metazoa. We then confirmed the results with more sensitive homology detection [54] followed by manual sequence analysis examining domain composition, which put the origin of LRPPRC and mS31 at the root of the Metazoa. Thus, the appearance of these proteins coincides with the loss of parts of the rRNA (Fig. 5a). SLIRP appears to originate slightly later than LRPPRC, but its small size makes determining its phylogenetic origin less conclusive.

The correlation between rRNA reduction and protein acquisition is important, because the rRNA regions h16 (410-432) and h33-37 (997-1118) that bridge the mRNA to the channel entrance in bacteria [8] are either absent or reduced in the metazoan mitoribosome. However, a superposition of the mitoribosome:LRPPRC-SLIRP-mRNA complex with *E. coli* expressome [8] shows not only

290 that the nascent mRNA follows a comparable path in both systems, but also the mRNA
291 delivering complexes bind in a similar location with respect to their ribosomes (Fig. 5b). To test
292 whether protein-protein interactions can explain the conservation, we compared the interface
293 with the *E. coli* expressome [8]. Indeed, in the expressome, NusG binds to uS10 and restrains
294 RNAP motions [8], and in our structure uS10m has a related interface between its α2 helix with
295 mS31-mS39, which induces association of these two proteins (Fig. 5c, Extended Data Fig. 7).
296 Yet, most of the interactions rely on a mitochondria-specific N-terminal extension of uS10m
297 where it shares a sheet with mS39 via the strand β1, and helices α1,16 and 18 are further
298 involved in the binding (Extended Data Fig. 7). A similar conclusion can be reached from
299 comparison with the *M. pneumoniae* expressome [10]. Together, this analysis suggests that a
300 specific protein-based mechanism must have evolved in the evolution of the metazoan
301 mitoribosome for mRNA recognition and protection.

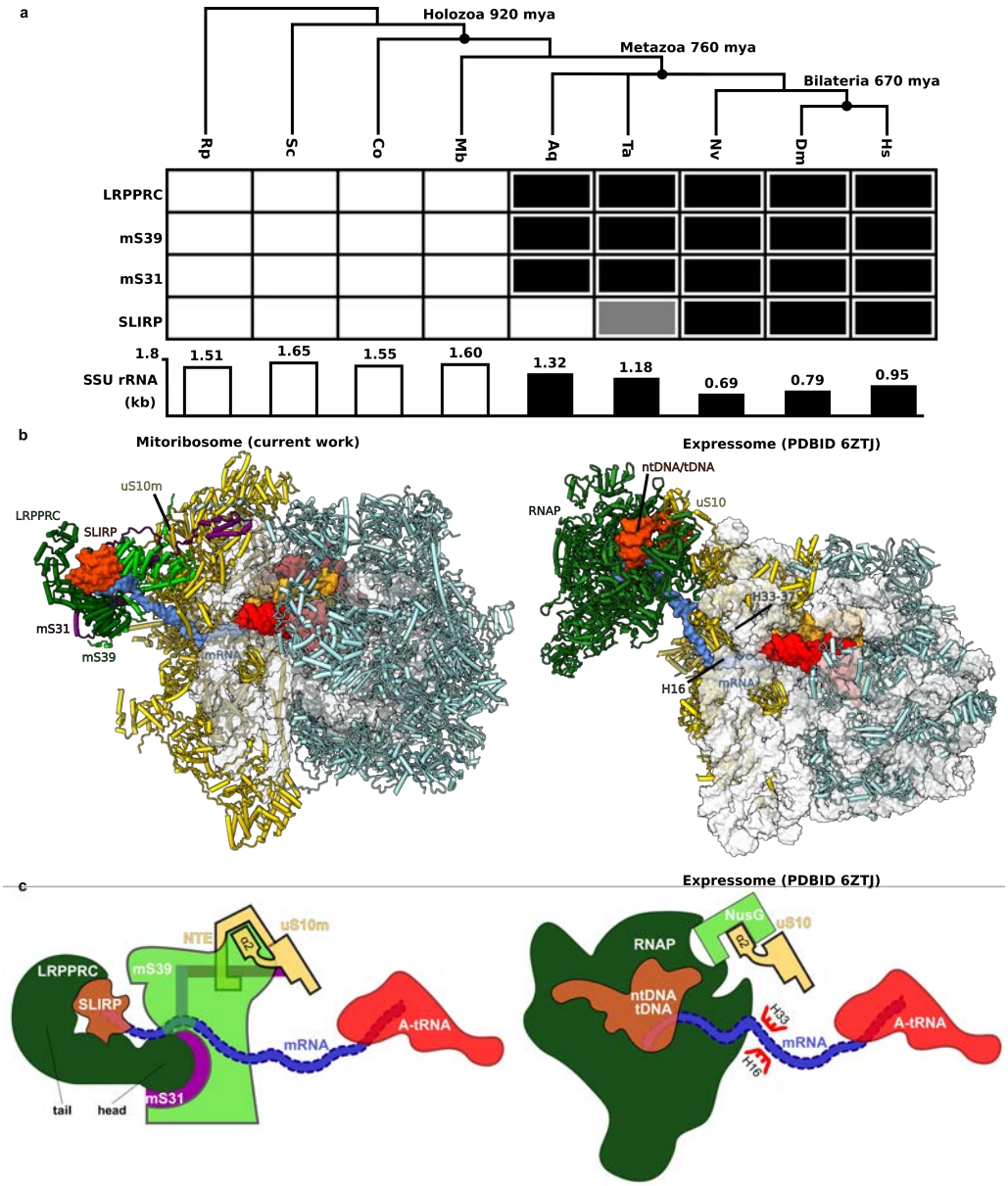

Figure 5. Formation of mitoribosome:LRPPRC-SLIRP and 70S:RNAP complexes. **a,** Phylogenetic analysis shows correlation between acquisition of LRPPRC, SLIRP, mS31, mS39 and reduction of rRNA in Metazoa. Black rectangles indicate the presence of proteins, grey indicates uncertainty about the presence of an ortholog. *Hs*: *Homo sapiens, Ds: Drosophila melanogaster, Nv*: *Nematostella vectensis, Ta: Trichoplax adhaerens, Aq*: *Amphimedon queenslandica* (sponge)*, Mb*: *Monosiga brevicollis* (unicellular choanoflagellate)*, Co*: *Capsaspora owczarzaki* (protist)*, Sc*: *Saccharomyces cerevisiae* (fungi)*, Rp*: *Rickettsia prowazekii* (alpha-proteobacterium). Dating in million years ago (mya) is based on previously described method [55]. **b,** Model of the mitoribosome:LRPPRC-SLIRP complex compared with the uncoupled model of the expressome from *E. coli* [8]. **c,** Schematic representation indicating association of mRNA-delivering proteins in the mitoribosome compared to NusG-coupled expressome [8].

315 **Discussion**

316 LRPPRC is an mRNA chaperone that regulates human mitochondrial transcription and
317 translation and is involved in a neurodegenerative disorder. In this study, we report the cryo-EM
318 structure of the LRPPRC-SLIRP in complex with the mitoribosome and characterize its function
319 with respect to the mRNA delivery. We identified that LRPPRC, in complex with SLIRP, binds
320 to mRNAs to hand-off transcripts to the mitoribosome for translation. The docking of LRPPRC
321 is realized through the mitoribosomal proteins mS39 and the N-terminus of mS31, that together
322 recognize eight of the LRPPRC helical repeats. The structural comparison with the unbound state
323 uncovers that the N-terminus of mS31 adopts a stable conformation upon LRPPRC association.

324 Our structure also shows that SLIRP is directly involved in interactions with mRNA. Those
325 interactions are supported by the comparison with other RNA-binding proteins that contain RNP
326 domains, similar to SLIRP. SLIRP further stabilizes the architecture of LRPPRC, and both are
327 required for mRNA binding. The mRNA is then channeled through a corridor formed with mS39
328 towards the decoding center.

329 Although *LRPPRC* knockout results in an overall decrease in the steady-state levels of the four
330 OXPHOS complexes that contain mtDNA-encoded subunits, by implementing an RNAseq
331 approach and metabolic labeling assays, we show that beyond its role in mRNA stabilization,
332 LRPPRC has differential effects on the translational efficiency of mitochondrial transcripts.
333 Specifically, the synthesis of ND1, ND2, ATP6, COX1, COX2, and COX3 are particularly
334 affected. Furthermore, our mitoribosome profiling data together with the structural analysis show
335 that LRPPRC-SLIRP does not preexist on the mitoribosome as a structural element. Thus, the
336 LRPPRC-SLIRP-dependent translation is not the sole regulatory pathway, and other mechanisms
337 involving mRNA binding are likely to co-exist.

338 Since mS39 and mS31 are specific to Metazoa, as well as LRPPRC-SLIRP, the proposed
339 mechanism in which some of the mitochondrial mRNAs are recruited for translation has
340 developed in a co-evolutionary manner in Metazoa. However, also the presence of large RNA-
341 binding moieties was also reported in association with mitoribosomes in other species [56-60].
342 Therefore, the principle of regulation by facilitation of molecular coupling might be a general
343 feature, while unique molecular connectors involved in different species.

344 Overall, these findings define LRPPRC-SLIRP as a regulator of mitochondrial gene expression
345 and explain how its components modulate the function of translation via mRNA binding. Given
346 the challenge of studying mitochondrial translation due to the lack of an *in vitro* system, the
347 native structures are crucial for explaining fundamental mechanisms. The identification of the
348 components involved enhances our understanding of mitochondrial translation. Together, these
349 studies provide the structural basis for translation regulation and activation in mitochondria.
350

351 **References**

352 1. Brown, A., Rathore, S., Kimanius, D., Aibara, S., Bai, X.-chen, Rorbach, J., Amunts, A., &
353 Ramakrishnan, V. Structures of the human mitochondrial ribosome in native states of
354 Assembly. *Nature Structural & Molecular Biology*, **24**(10), 866–869 (2017).

355 2. Sissler, M., & Hashem, Y. Mitoribosome assembly comes into view. *Nature Structural &*
356 *Molecular Biology*, **28**(8), 631–633 (2021).

357 3. Itoh, Y. *et al.* Mechanism of mitoribosomal small subunit biogenesis and preinitiation.
358 *Nature* **606,** 603–608 (2022).

359 4. Lavdovskaia, E., Hillen, H. S., & Richter-Dennerlein, R. Hierarchical folding of the catalytic
360 core during mitochondrial ribosome biogenesis. *Trends in Cell Biology*, **32**(3), 182-185
361 (2022).

362 5. Harper, N.J., Burnside, C. & Klinge, S. Principles of mitoribosomal small subunit assembly
363 in eukaryotes. *Nature* **614**, 175–181 (2023).

364 6. Khawaja, A. *et al.* Distinct pre-initiation steps in human mitochondrial translation. *Nat*
365 *Commun* **11**, 2932, (2020).

366 7. Rackham, O., Filipovska, A. Organization and expression of the mammalian mitochondrial
367 genome. *Nat Rev Genet*. **10**, 606-623 (2022).

368 8. Webster, M. W. *et al.* Structural basis of transcription-translation coupling and collision in
369 bacteria. *Science* **369,** 1355–1359 (2020).

370 9. Wang, C. *et al.* Structural basis of transcription-translation coupling. *Science* **369,** 1359–
371 1365 (2020).

372 10. O'Reilly, F. J. *et al.* In-cell architecture of an actively transcribing-translating expressome.
373 *Science* **369,** 554–557 (2020).

374 11. Itoh, Y. *et al.* Mechanism of membrane-tethered mitochondrial protein synthesis. *Science*
375 **371,** 846–849 (2021).
376 12. Ott, M., Amunts, A. & Brown, A. Organization and regulation of mitochondrial protein
377 synthesis. *Annual Review of Biochemistry* **85,** 77–101 (2016).
378 13. Christian, B. and Spremulli, L. Preferential selection of the 5′-terminal start codon on
379 leaderless mRNAs by mammalian mitochondrial ribosomes *J Biol Chem* **285**, 28379-28386
380 (2010).
381 14. Yi, SH. *et al.* Conformational rearrangements upon start codon recognition in human 48S
382 translation initiation complex. *Nucleic Acid Research* **50**, 5282–5298 (2022).
383 15. Lapointe, C.P. *et al.* eIF5B and eIF1A reorient initiator tRNA to allow ribosomal subunit
384 joining. *Nature*, **607** (7917) 185-190 (2022).
385 16. Ruzzenente, B. *et al.* LRPPRC is necessary for polyadenylation and coordination of
386 translation of mitochondrial mrnas. *The EMBO Journal* **31,** 443–456 (2012).
387 17. Siira, S. J. *et al.* LRPPRC-mediated folding of the mitochondrial transcriptome. *Nature*
388 *Communications* **8,** (2017).
389 18. Chujo, T. *et al.* LRPPRC/SLIRP suppresses pnpase-mediated mrna decay and promotes
390 polyadenylation in human mitochondria. *Nucleic Acids Research* **40,** 8033–8047 (2012).
391 19. Sasarman, F., Brunel-Guitton, C., Antonicka, H., Wai, T. & Shoubridge, E. A. LRPPRC and
392 SLIRP interact in a ribonucleoprotein complex that regulates posttranscriptional gene
393 expression in mitochondria. *Molecular Biology of the Cell* **21,** 1315–1323 (2010).
394 20. Mootha, V. K. *et al.* Identification of a gene causing human cytochrome *c* oxidase
395 deficiency by Integrative Genomics. *Proceedings of the National Academy of Sciences* **100,**
396 605–610 (2003).
397 21. Antonicka, H. *et al*. A high-density human mitochondrial proximity interaction network.
398 *Cell Metab* **32**, 479-497 (2020).
399 22. Sasarman, F., Brunel-Guitton, C., Antonicka, H., Wai, T. & Shoubridge, E.A. LRPPRC and
400 SLIRP interact in a ribonucleoprotein complex that regulates posttranscriptional gene
401 expression in mitochondria. *Mol. Biol. Cell* **21**, 1315-1323. (2010).

402 23. Lagouge, M. *et al.* SLIRP regulates the rate of mitochondrial protein synthesis and protects
403 LRPPRC from degradation. *PLOS Genetics* **11,** (2015).
404 24. Baughman, J. M. *et al.* A computational screen for regulators of oxidative phosphorylation
405 implicates SLIRP in mitochondrial RNA homeostasis. *PLoS Genetics* **5,** (2009).
406 25. Guo, L. *et al.* Pathogenic SLIRP variants as a novel cause of autosomal recessive
407 mitochondrial encephalomyopathy with complex I and IV deficiency. *European Journal of*
408 *Human Genetics* **29,** 1789–1795 (2021).
409 26. Sasarman, F. *et al.* Tissue-specific responses to the LRPPRC founder mutation in French
410 Canadian leigh syndrome. *Human Molecular Genetics* **24,** 480–491 (2014).
411 27. Xu, F., Addis, J. B. L., Cameron, J. M. & Robinson, B. H. LRPPRC mutation suppresses
412 cytochrome oxidase activity by altering mitochondrial RNA transcript stability in a mouse
413 model. *Biochemical Journal* **441,** 275–283 (2011).
414 28. Spåhr, H. *et al.* SLIRP stabilizes LRPPRC via an RRM–PPR protein interface. *Nucleic*
415 *Acids Research* **44,** 6868–6882 (2016).
416 29. Soto, I. *et al.* Balanced mitochondrial and cytosolic translatomes underlie the biogenesis of
417 human respiratory complexes. *Genome Biol.* **23**, 170 (2022).
418 30. Aibara, S., Singh, V., Modelska, A. & Amunts, A. Structural basis of mitochondrial
419 translation. *eLife* **9,** (2020).
420 31. Amunts, A., Brown, A., Toots, J., Scheres, S. H. & Ramakrishnan, V. The structure of the
421 human mitochondrial ribosome. *Science* **348,** 95–98 (2015).
422 32. Greber, B. J. *et al.* The complete structure of the 55S mammalian mitochondrial ribosome.
423 *Science* **348,** 303–308 (2015).
424 33. Itoh, Y., *et al.* Structure of the mitoribosomal small subunit with streptomycin reveals Fe-S
425 clusters and physiological molecules *eLife* 11:e77460 (2022).
426 34. Jumper J, *et al*. Highly accurate protein structure prediction with Alphafold. *Nature* **596,**
427 583–589 (2021).
428 35. Painter, Jay, and Ethan A. Merritt. "Optimal description of a protein structure in terms of
429 multiple groups undergoing TLS motion." *Acta Crystallographica Section D: Biological*
430 *Crystallography* **62,** 439-450 (2006).

431 36. Painter, Jay, and Ethan A. Merritt. "TLSMD web server for the generation of multi-group
432 TLS models." *Journal of applied crystallography* **39,** 109-111 (2006).
433 37. Coquille, S. & Thore, S. Leigh syndrome-inducing mutations affect LRPPRC / SLIRP
434 complex formation. *bioRxiv* https://doi.org/10.1101/2020.04.16.044412 (2020).
435 38. Burd, C. G., & Dreyfuss, G. Conserved structures and diversity of functions of RNA-
436 binding proteins. *Science*, **265,** 615-621 (1994).
437 39. Hatchell, E. C., Colley, S. M., Beveridge, D. J., Epis, M. R., Stuart, L. M., Giles, K. M., ... &
438 Leedman, P. J. SLIRP, a small SRA binding protein, is a nuclear receptor corepressor.
439 *Molecular cell*, **22,** 657-668 (2006).
440 40. Johansson, C., Finger, L. D., Trantirek, L., Mueller, T. D., Kim, S., Laird-Offringa, I. A., &
441 Feigon, J. Solution structure of the complex formed by the two N-terminal RNA-binding
442 domains of nucleolin and a pre-rRNA target. *Journal of molecular biology*, **337,** 799-816
443 (2004).
444 41. Williams, P., Li, L., Dong, X., & Wang, Y. Identification of SLIRP as a G quadruplex-
445 binding protein. *Journal of the American Chemical Society*, **139,** 12426-12429 (2017).
446 42. Deo, R. C., Bonanno, J. B., Sonenberg, N., & Burley, S. K. Recognition of polyadenylate
447 RNA by the poly (A)-binding protein. *Cell*, **98,** 835-845 (1999).
448 43. Wu, B., Su, S., Patil, D. P., Liu, H., Gan, J., Jaffrey, S. R., & Ma, J. Molecular basis for the
449 specific and multivariant recognitions of RNA substrates by human hnRNP A2/B1. *Nature*
450 *communications*, **9,** 1-12 (2018).
451 44. Takyar, S., Hickerson, R. P., & Noller, H. F. mRNA helicase activity of the ribosome. *Cell*,
452 **120**, 49–58 (2005).
453 45. Umate, P., Tuteja, N., & Tuteja, R. Genome-wide comprehensive analysis of human
454 helicases. *Communicative & Integrative Biology*, **4**, 118–137 (2011).
455 46. Kummer E, Leibundgut M, Rackham O, Lee RG, Boehringer D, Filipovska A & Ban N.
456 Unique features of mammalian mitochondrial translation initiation revealed by cryo-EM
457 *Nature* **560**, 263-267 (2018).
458 47. Xu, F., Morin, C., Mitchell, G., Ackerley, C. & Robinson, B.H. The role of the *LRPPRC*
459 (leucine-rich pentatricopeptide repeat cassette) gene in cytochrome oxidase assembly:
460 mutation causes lowered levels of COX (cytochrome c oxidase) I and *COX III* mRNA.
461 *Biochem J.* **382**, 331-336. (2004).

462 48. Ruzzenente, B. *et al.* LRPPRC is necessary for polyadenylation and coordination of
463 translation of mitochondrial mRNAs. *EMBO J.* **31**, 443-456 (2012).
464 49. Couvillion, M.T., Soto, I.C., Shipkovenska, G. & Churchman, L.S. Synchronized
465 mitochondrial and cytosolic translation programs. *Nature* **533**, 499-503 (2016).
466 50. Ingolia, N.T., Ghaemmaghami, S., Newman, J.R. & Weissman, J.S. Genome-wide analysis
467 in vivo of translation with nucleotide resolution using ribosome profiling. *Science* **324**, 218-
468 223 (2009).
469 51. Petrov, A. S. *et al.* Structural patching fosters divergence of mitochondrial ribosomes.
470 *Molecular Biology and Evolution* **36,** 207–219 (2018).
471 52. Huerta-Cepas, J. *et al.* Eggnog 5.0: A hierarchical, functionally and phylogenetically
472 annotated orthology resource based on 5090 organisms and 2502 viruses. *Nucleic Acids*
473 *Research* **47,** (2018).
474 53. Sterky, F. H., Ruzzenente, B., Gustafsson, C. M., Samuelsson, T. & Larsson, N.-G.
475 LRPPRC is a mitochondrial matrix protein that is conserved in metazoans. *Biochemical and*
476 *Biophysical Research Communications* **398,** 759–764 (2010).
477 54. Eddy, S. R. Accelerated profile HMM searches. *PLoS Computational Biology* **7,** (2011).
478 55. Erwin, D. H. Early metazoan life: divergence, environment and ecology. *Philosophical*
479 *Transactions of the Royal Society B: Biological Sciences*, **370,** 1-7 (2015).
480 56. Amunts, A. *et al.* Structure of the yeast mitochondrial large ribosomal subunit. *Science* **343,**
481 1485–1489 (2014).
482 57. Tobiasson, V. & Amunts, A. Ciliate mitoribosome illuminates evolutionary steps of
483 mitochondrial translation. *eLife* **9,** (2020).
484 58. Waltz, F., Soufari, H., Bochler, A., Giegé, P. & Hashem, Y. Cryo-EM structure of the RNA-
485 rich plant mitochondrial ribosome. *Nature Plants* **6,** 377–383 (2020).
486 59. Waltz, F. *et al.* How to build a ribosome from RNA fragments in Chlamydomonas
487 mitochondria. *Nature Communications* **12,** (2021).
488 60. Tobiasson, V., Berzina, I. & Amunts, A. Structure of a mitochondrial ribosome with
489 fragmented rRNA in complex with membrane-targeting elements. *Nature Communications*
490 **13,** 6132 (2022).
491

492 **Methods**

493 Experimental model and culturing

494 HEK293S-derived cells (T501) were grown in Freestyle 293 Expression Medium containing 5%
495 tetracycline-free fetal bovine serum (FBS) in vented shaking flasks at 37°C, 5% CO_2 and 120
496 rpm (550 x g). Culture was scaled up sequentially, by inoculating at 1.5 x 10^6 cells/mL and
497 subsequently splitting at a cell density of 3.0 x 10^6 cells/mL. Finally, a final volume of 2 L of cell
498 culture at a cell density of 4.5 x 10^6 cells/mL was used for mitochondria isolation, as previously
499 described [61].

500

501 Mitoribosome purification

502 HEK293S-derived cells were harvested from the 2 L culture when the cell density was 4.2 x 10^6
503 cells/mL by centrifugation at 1,000 g for 7 min, 4 °C. The pellet was washed and resuspended in
504 200 mL Phosphate Buffered Saline (PBS). The washed cells were pelleted at 1,000 g for 10 min
505 at 4 °C. The resulting pellet was resuspended in 120 mL of MIB buffer (50 mM HEPES-KOH,
506 pH 7.5, 10 mM KCl, 1.5 mM $MgCl_2$, 1 mM EDTA, 1 mM EGTA, 1 mM dithiothreitol,
507 cOmplete EDTA-free protease inhibitor cocktail (Roche) and allowed to swell in the buffer for
508 15 min in the cold room by gentle stirring. About 45 mL of SM4 buffer (840 mM mannitol, 280
509 mM sucrose, 50 mM HEPES-KOH, pH 7.5, 10 mM KCl, 1.5 mM $MgCl_2$, 1 mM EDTA, 1 mM
510 EGTA, 1 mM DTT, 1X cOmplete EDTA-free protease inhibitor cocktail (Roche) was added to
511 the cells in being stirred in MIB buffer and poured into a nitrogen cavitation device kept on ice.
512 The cells were subjected to a pressure of 500 psi for 20 min before releasing the nitrogen from
513 the chamber and collecting the lysate. The lysate was clarified by centrifugation at 800 x g and 4
514 °C, for 15 min, to separate the cell debris and nuclei. The supernatant was passed through a
515 cheesecloth into a beaker kept on ice. The pellet was resuspended in half the previous volume of
516 MIBSM buffer (3 volumes MIB buffer + 1 volume SM4 buffer) and homogenized with a
517 Teflon/glass Dounce homogenizer. After clarification as described before, the resulting lysate
518 was pooled with the previous batch of the lysate and subjected to centrifugation at 1,000 x g, 4
519 °C for 15 minutes to ensure complete removal of cell debris. The clarified and filtered
520 supernatant was centrifuged at 10,000 x g and 4 °C for 15 min to pellet crude mitochondria.
521 Crude mitochondria were resuspended in 10 mL MIBSM buffer and treated with 200 units of

522 Rnase-free Dnase (Sigma-Aldrich) for 20 min in the cold room to remove contaminating
523 genomic DNA. Crude mitochondria were again recovered by centrifugation at 10,000 g, 4 °C for
524 15 min and gently resuspended in 2 mL SEM buffer (250 mM sucrose, 20 mM HEPES-KOH,
525 pH 7.5, 1 mM EDTA). Resuspended mitochondria were subjected to a sucrose density step-
526 gradient (1.5 mL of 60% sucrose; 4 mL of 32% sucrose; 1.5 mL of 23% sucrose and 1.5 mL of
527 15% sucrose in 20 mM HEPES-KOH, pH 7.5, 1 mM EDTA) centrifugation in a Beckmann
528 Coulter SW40 rotor at 28,000 rpm (139,000 x g) for 60 min. Mitochondria seen as a brown band
529 at the interface of 32% and 60% sucrose layers were collected and snap-frozen using liquid
530 nitrogen and transferred to −80 °C.

531 Frozen mitochondria were transferred on ice and allowed to thaw slowly. Lysis buffer (25 mM
532 HEPES-KOH, pH 7.5, 50 mM KCl, 10 mM $Mg(Oac)_2$, 2% polyethylene glycol octylphenyl
533 ether, 2 mM DTT, 1 mg/mL EDTA-free protease inhibitors (Sigma-Aldrich) was added to
534 mitochondria and the tube was inverted several times to ensure mixing. A small Teflon/glass
535 Dounce homogenizer was used to homogenize mitochondria for efficient lysis. After incubation
536 on ice for 5-10 min, the lysate was clarified by centrifugation at 30,000 x g for 20 min, 4 °C. The
537 clarified lysate was carefully collected. Centrifugation was repeated to ensure complete
538 clarification. A volume of 1 mL of the mitochondrial lysate was applied on top of 0.4 mL of 1 M
539 sucrose (v/v ratio of 2.5:1) in thick-walled TLS55 tubes. Centrifugation was carried out at
540 231,500 x g for 45 min in a TLA120.2 rotor at 4 °C. The pellets thus obtained were washed and
541 sequentially resuspended in a total volume of 100 µl resuspension buffer (20 mM HEPES-KOH,
542 pH 7.5, 50 mM KCl, 10 mM $Mg(Oac)_2$, 1% Triton X-100, 2 mM DTT). The sample was
543 clarified twice by centrifugation at 18,000 g for 10 min at 4 °C. The sample was applied on to a
544 linear 15-30% sucrose (20 mM HEPES-KOH, pH 7.5, 50 mM KCl, 10 mM $Mg(Oac)_2$, 0.05% n-
545 dodecyl-β-D-maltopyranoside, 2 mM DTT) gradient and centrifuged in a TLS55 rotor at 213,600
546 x g for 120 min at 4 °C. The gradient was fractionated into 50 µL volume aliquots. The
547 absorption for each aliquot at 260 nm was measured and fractions corresponding to the
548 monosome peak were collected. The pooled fractions were subjected to buffer exchange with the
549 resuspension buffer.

550

551 <u>Cryo-EM data acquisition</u>

552 3 µL of ~120 nM mitoribosome was applied onto a glow-discharged (20 mA for 30 sec) holey-
553 carbon grid (Quantifoil R2/2, copper, mesh 300) coated with continuous carbon (of ~3 nm
554 thickness) and incubated for 30 sec in a controlled environment of 100% humidity and 4 ºC. The
555 grids were blotted for 3 sec, followed by plunge-freezing in liquid ethane, using a Vitrobot
556 MKIV (ThermoFischer). The data were collected on FEI Titan Krios (ThermoFischer)
557 transmission electron microscope operated at 300 keV, using C2 aperture of 70 µm and a slit
558 width of 20 eV on a GIF quantum energy filter (Gatan). A K2 Summit detector (Gatan) was used
559 at a pixel size of 0.83 Å (magnification of 165,000X) with a dose of 29-32 electrons/$Å^2$
560 fractionated over 20 frames.

561

562 Cryo-EM data processing

563 The beam-induced motion correction and per-frame B-factor weighting were performed using
564 RELION-3.0.2 [62,63]. Motion-corrected micrographs were used for contrast transfer function
565 (CTF) estimation with gctf [64]. Unusable micrographs were removed by manual inspection of the
566 micrographs and their respective calculated CTF parameters. Particles were picked in RELION-
567 3.0.2, using reference-free followed by reference-aided particle picking procedures. Reference-
568 free 2D classification was carried out to sort useful particles from falsely picked objects, which
569 were then subjected to 3D classification. 3D classes corresponding to unaligned particles and
570 LSU were discarded, and monosome particles were pooled and used for 3D auto-refinement
571 yielding a map with an overall resolution of 2.9-3.4 Å for the five datasets. Resolution was
572 estimated using a Fourier Shell Correlation cut-off of 0.143 between the two reconstructed half
573 maps. Finally, the selected particles were subjected to per-particle defocus estimation, beam-tilt
574 correction, and per-particle astigmatism correction followed by Bayesian polishing. Bayesian
575 polished particles were subjected to a second round per-particle defocus correction. A total of
576 994,919 particles were pooled and separated into 86 optics groups in RELION-3.1 [65], based on
577 acquisition areas and date of data collection. Beam-tilt, magnification anisotropy, and higher-
578 order (trefoil and fourth-order) aberrations were corrected in RELION-3.1 [65]. Particles with A-
579 site and/or P-site occupied with tRNAs which showed comparatively higher occupancy for the
580 unmodeled density potentially corresponding to the LRPPRC-SLIRP module, were pooled and
581 re-extracted in a larger box size of 640 Å. The re-extracted particles were subjected to 3D
582 autorefinement in RELION3.1 [65]. This was followed by sequential signal subtraction to remove

583 signal from the LSU, and all of the SSU except the region around mS39 and the unmodeled
584 density, in that order. The subtracted data was subjected to masked 3D classification (T=200) to
585 enrich for particles carrying the unmodeled density. Using a binary mask covering mS39 and all
586 of the unmodeled density, we performed local-masked refinement on resulting 41,812 particles
587 within an extracted sub-volume of 240 Å box size leading to 3.37 Å resolution map.

588

589 Model building and refinement

590 At the mRNA channel entrance, a more accurate and complete model of mS39 could be built
591 with 29 residues added to the structure. Improved local resolution enabled unambiguous
592 assignment of residues to the density which allowed us to address errors in the previous model.
593 A total of 28 α-helices could be modeled in their correct register and orientation. Further, a 28-
594 residue long N-terminal loop of mS31 (residues 247–275) along mS39 and mito-specific N-
595 terminal extension of uS9m (residues 53–70) approaching mRNA were modeled by fitting the
596 loops in to the density maps.

597 For building LRPPRC-SLIRP module, the initial model of the full length LRPPRC was obtained
598 from *AlphaFold2* Protein Structure Database (Uniprot ID P42704). Based on the analysis, three
599 stable domains were identified that are connected by flexible linkers (673-983, 1035-1390). We
600 then systematically assessed the domains against the map, and the N-terminal region (77-660)
601 could be fitted into the density. The initial model was real space refined into the 3.37 Å
602 resolution map of mS39-LRPPRC-SLIRP region obtained after partial signal subtraction using
603 reference-restraints in *Coot* v0.9 [66]. The N-terminal region covering residues 64-76 was
604 identified in the density map and allowed us to model 34 helices of LRPPRC (residues 64-644).
605 Helices α1-29 could be confidently modeled. An additional five helices, as predicted by
606 *Alphafold2* [34], could be accommodated into the remaining density. After modelling LRPPRC into
607 the map, there was an unaccounted density that fits SLIRP. The initial model of SLIRP was
608 obtained from *Alphafold2* Protein Structure Database (Uniprot ID Q9GZT3). The unmodeled
609 density agreed with the secondary structure of SLIRP. The model was real space refined into the
610 density using reference-restraints as was done for LRPPRC in *Coot* v0.9 [66]. Five additional RNA
611 residues could be added to the 3' terminal of mRNA to account for tubular density extending
612 from it along the mRNA binding platform. The A/A P/P E/E state model was rigid body fitted

613 into the corresponding 2.85 Å resolution consensus map. Modeled LRPPRC was merged with
614 the rigid body fitted monosome model to obtain a single model of the mitoribosome bound to
615 LRPPRC and SLIRP. The model was then refined against the composite map using PHENIX
616 v1.18 [67] (Supplementary Information Table 1).

617

618 Phylogenetic analysis

619 Phylogenetic distribution of proteins was determined by examining phylogeny databases [55],
620 followed by sensitive homology detection to detect homologs outside of the bilateria. Orthologs
621 were required to have identical domain compositions, and Dollo parsimony was used to infer the
622 evolutionary origin of a protein from its phylogenetic distribution. When multiple homologs of a
623 protein were detected in a species, a neighbor-joining phylogeny was constructed to assess
624 monophyly of putative orthologs to the human protein. The short length of the SLIRP candidate
625 protein from *T. adhaerens* (B3SAC0_TRIAD), that is part of the large RRM family, precludes
626 obtaining a reliable phylogeny to confidently assess its orthology to human SLIRP is therefore
627 tentative.

628

629 TLSMD analysis

630 The TLSMD analysis [35,36] was performed with full length LRPPRC model obtained from
631 AlphaFold Database (AF-P42704-F1), and mitochondrial targeting sequence (residues 1-59) was
632 removed. The model was divided into TLS segments (N), and single chain TLSMD is performed
633 on all atoms using the isotropic analysis model. Instead of using atomic B-factors, the values for
634 a per residue confidence score of AlphaFold called predicted local distance difference test
635 (pLDDT) were used as reference to calculate the least squared residuals against the
636 corresponding values calculated by TLSMD analysis. This is based on the assumption that local
637 mobility of the model should be inversely correlated with the pLDDT score. AlphaFold pLDDT
638 values and the corresponding calculated values were plotted for every iteration to monitor
639 improvement in prediction and across the length of LRPPRC. The data in Extended Data Fig. 2
640 is presented for N=4, where segments 1 and 2 (residues 60-373 and 374-649) correspond to the
641 modeled region, whereas segments 3 and 4 correspond to the remaining domains that could not
642 be modeled.

643

644 Helicase sequence analysis

645 To address the possibility that LRPPRC may serve as a helicase, we inspected the sequence of
646 full-length LRPPRC (Uniprot ID P42704). First, we checked the sequence for matches with
647 consensus motifs characteristic of helicases using regular expression search. The following
648 motifs were searched, GFxxPxxIQ, AxxGxGKT, PTRELA, TPGR, DExD, SAT, FVxT, RgxD
649 (DDX helicases); GxxGxGKT, TQPRRV, TDGML, DExH, SAT, FLTG, TNIAET, QrxGRAGR
650 (DHX helicases); AHTSAGKT, TSPIKALSNQ, MTTEIL (others). Next, we carried out multiple
651 sequence analysis against representative member helicases of the DHX and DDX family to
652 verify the results of the regular-expression sequence search and to find potentially valid weaker
653 matches.

654

655 Human cell lines and cell culture conditions

656 Human HEK293T embryonic kidney cells (CRL-3216, RRID: CVCL-0063) were obtained from
657 ATCC. The HEK293T *LRPPRC* knock-out (KO) cell line was engineered in-house and
658 previously reported [27]. The LRPPRC-KO cell line was reconstituted with either the wild-type
659 *LRPPRC* gene [27], or a variant causing Leigh syndrome, French-Canadian type (LSFC). The
660 LSFC variant carries a single base change (nucleotide C1119T transition), predicting a missense
661 A354V change at a conserved protein residue [46].
662 Cells were cultured in high-glucose Dulbecco's modified Eagle's medium (DMEM, Thermo
663 Fisher Scientific, CAT 11965092), supplemented with 10% FBS (Thermo Fisher Scientific, CAT
664 A3160402), 100 µg/mL of uridine (Sigma, CAT U3750), 3 mM sodium formate (Sigma CAT
665 247596), and 1 mM sodium pyruvate (Thermo Fisher Scientific, CAT 11360070) at 37 °C under
666 5% CO_2. Cell lines were routinely tested for mycoplasma contamination.
667 To generate an *LRPPRC*-KO cell line reconstituted with the LSFC variant of the gene, a Myc-
668 DDK tagged *LRPPRC* ORF plasmid was obtained from OriGene (CAT: RC216747). This ORF
669 was then subcloned into a hygromycin resistance-containing pCMV6 entry vector (OriGene,
670 CAT PS100024) and used to generate an *LRPPRC*-KO cell line reconstituted with a wild-type
671 *LRPPRC* gene as reported [27]. To generate the *LRPPRC*-LSFC variant carrying the C1119T
672 mutation, we used the Q5® Site-Directed Mutagenesis Kit from NEB. ~ 10 pg of template
673 pCMV6-A-Myc-DDK-Hygro-*LRPPRC* vector were used, along with the primers LSFC-Q5-F 5'

674 GGAAGATGTAGTGTTGCAGATTTTAC and LSFC-Q5-R 5'
675 AATTTTTCAGTGACTAAAAGTAAAATG, designed to include the codon to be mutated.
676 After exponential amplification and treatment with kinase and ligase, 2.5 µl of the reaction were
677 transformed into competent *Escherichia coli* cells. Several transformants were selected, their
678 plasmid DNA purified, and then sequenced to select the correct pCMV6-A-Myc-DDK-Hygro-
679 *LRPPRC-LSFC* construct.
680 For transfection of the construct into *LRPPRC*-KO cells, we used 5 µl of EndoFectin mixed with
681 2 µg of vector DNA in OptiMEM-I media according to the manufacturer's instructions. Media
682 was supplemented with 200 µg/ml of hygromycin after 48 h, and drug selection was maintained
683 for at least one month.
684
685 Whole-Cell extracts and Mitochondria isolation
686 For SDS-PAGE electrophoresis, pelleted cells were solubilized in RIPA buffer (25 mM Tris-HCl
687 pH 7.6, 150 mM NaCl, 1% NP-40, 1% sodium deoxycholate, and 0.1% SDS) with 1 mM PMSF
688 (phenylmethylsulfonyl fluoride) and mammalian protease inhibitor cocktail (Sigma). Whole-cell
689 extracts were cleared by 5 min centrifugation at 20,000 x *g* at 4 °C.
690 Mitochondria-enriched fractions were isolated from at least ten 80% confluent 15-cm plates as
691 described previously [68-70]. Briefly, the cells were resuspended in ice-cold T-K-Mg buffer (10 mM
692 Tris–HCl, 10 mM KCl, 0.15 mM $MgCl_2$, pH 7.0) and disrupted with 10 strokes in a homogenizer
693 (Kimble/Kontes, Vineland, NJ). Using a 1 M sucrose solution, the homogenate was brought to a
694 final concentration of 0.25 M sucrose. A post-nuclear supernatant was obtained by centrifugation
695 of the samples twice for 5 min at 1,000 x *g*. Mitochondria were pelleted by centrifugation for 10
696 min at 10,000 x *g* and resuspended in a solution of 0.25 M sucrose, 20 mM Tris-HCl, 40 mM
697 KCl, and 10 mM $MgCl_2$, pH 7.4.
698
699 Denaturing and native electrophoresis, followed by immunoblotting
700 Protein concentration was measured by the Lowry method [71]. 40–80 µg of mitochondrial protein
701 extract was separated by denaturing SDS–PAGE in the Laemmli buffer system [72]. Then, proteins
702 were transferred to nitrocellulose membranes and probed with specific primary antibodies
703 against the following proteins: β-ACTIN (dilution 1:2,000; Proteintech; Rosemont, IL; 60008-1-
704 Ig), ATP5A (1:1000; Abcam; Cambridge, MA; ab14748), CORE2 (1:1,000; Abcam; Cambridge,

705 MA; ab14745), COX1 (dilution 1:2,000; Abcam; Cambridge, MA; ab14705), LRPPRC (dilution
706 1:1,000; Proteintech; Rosemont, IL; 21175-1-AP), NDUFA9 (1:1000; Proteintech; Rosemont,
707 IL; 20312-1-AP), SDHA (1:1,000; Proteintech; Rosemont, IL; 14865-1-AP) or SLIRP (1:1000;
708 Abcam; Cambridge, MA; ab51523). Horseradish peroxidase-conjugated anti-mouse or anti-
709 rabbit IgGs were used as secondary antibodies (dilution 1:10,000; Rockland; Limerick, PA). β-
710 ACTIN was used as a loading control. Signals were detected by chemiluminescence incubation
711 and exposure to X-ray film.
712 Blue-native polyacrylamide gel electrophoresis (BN-PAGE) analysis of mitochondrial OXPHOS
713 complexes in native conditions was performed as described previously [73,74]. To extract
714 mitochondrial proteins in native conditions, we pelleted and solubilized 400 µg mitochondria in
715 100 µl buffer containing 1.5 M aminocaproic acid and 50 mM Bis-Tris (pH 7.0) with 1% n-
716 dodecyl b-D-maltoside (DDM). Solubilized samples were incubated on ice for 10 min in ice and
717 pelleted at 20,000 x *g* for 30 min at 4 °C. The supernatant was supplemented with 10 µl of
718 sample buffer 10X (750 mM aminocaproic acid, 50 mM Bis-Tris, 0.5 mM EDTA
719 (ethylenediaminetetraacetic acid), 5% Serva Blue G-250). Native PAGE™ Novex® 3-12% Bis-
720 Tris Protein Gels (Thermo Fisher) gels were loaded with 40 µg of mitochondrial proteins. After
721 electrophoresis, the gel was stained with 0.25% Coomassie brilliant blue R250, or proteins were
722 transferred to PVDF membranes using an eBlot L1 protein transfer system (GenScript,
723 Piscataway, NJ) and used for immunoblotting.
724
725 Pulse Labeling of Mitochondrial Translation Products
726 To determine mitochondrial protein synthesis, 6-well plates were pre-coated at 5 µg/cm^2 with 50
727 µg/mL collagen in 20 mM acetic acid and seeded with WT or LRPPRC cell lines (two wells per
728 sample per timepoint). 70% confluent cell cultures were incubated for 30 min in DMEM without
729 methionine and then supplemented with 100 µl/ml emetine for 10 min to inhibit cytoplasmic
730 protein synthesis as described [68]. 100 µCi of [^{35}S]-methionine was added and allowed to
731 incorporate to newly synthesized mitochondrial proteins for increasing times from 15- to 60-
732 minute pulses. Subsequently, whole-cell extracts were prepared by solubilization in RIPA buffer,
733 and equal amounts of total cellular protein were loaded in each lane and separated by SDS-
734 PAGE on a 17.5% polyacrylamide gel. Gels were transferred to a nitrocellulose membrane and
735 exposed to a Kodak X-OMAT X-ray film. The membranes were then probed with a primary

736 antibody against β-ACTIN as a loading control. Optical densities of the immunoreactive bands
737 were measured using the Histogram function of the Adobe Photoshop software in digitalized
738 images.
739
740 Whole-cell transcriptomics
741 Cells were grown to 80% confluency in a 10 cm plate (two plates per sample) and were collected
742 by trypsinization and washed once with PBS before resuspending in one mL of Trizol
743 (ThermoFisher Scientific). RNA was extracted following the Trizol manufacturer's
744 specifications. The aqueous phase was transferred to a new tube, and an equal volume of 100%
745 isopropanol and 3 µL of glycogen were added to precipitate the RNA. The sample was incubated
746 at -80 ºC overnight and centrifuged at 15,000 x*g* for 45 min at 4°C. RNA was resuspended in 50
747 µL of RNAse-free water and quantified by measuring absorbance at a wavelength of 260 nm. 2
748 µg of RNA was sent to Novogene (Sacramento, CA) for further processing. Novogen services
749 included library preparation, RNA sequencing (RNAseq) on an Illumina HiSeq platform
750 according to the Illumina Tru-Seq protocol, and bioinformatics analysis. The raw data was
751 cleaned to remove low-quality reads and adapters using Novogen in-house Perl scripts in
752 Cutadapt [75]. The reads were mapped to the reference genome using the HISAT2 software [76]. The
753 transcripts were assembled and merged to obtain an mRNA expression profile with the StringTie
754 algorithm [77], the RNA-seq data was then normalized to account for the total reads sequenced for
755 each sample (the read depth), and differentially expressed mRNAs were identified by using the
756 Ballgown suite [78] and the DESeq2 R package [79]. GraphPad Prism version 9.0 software
757 (GraphPad Software, San Diego, CA, USA) was used to prepare the volcano plots.
758
759 Mitoribosome profiling
760 Mitoribosome profiling, matched RNA-seq, and data analysis were performed as described [29].
761 Briefly, human and mouse cell lysates were prepared and mixed 95:5 human:mouse. For
762 mitoribosome profiling, the combined lysates were subjected to RNaseI treatment and
763 fractionated across a linear sucrose gradient. Sequencing libraries were prepared from the
764 monosome fraction after phenol/chloroform extraction. For RNA-seq, RNA was extracted from
765 the undigested combined lysate, fragmented by alkaline hydrolysis, and sequencing libraries
766 prepared. Reads were cleaned of adapters, filtered of rRNA fragments, and PCR duplicates were

767 removed. Read counts were summed across features (coding sequences) using Rsubread feature
768 Counts [80], then normalized by feature length and mouse spike-in read counts. TE was calculated
769 by dividing spike-in normalized mitoRPF reads per kilobase by spike-in normalized RNA-seq
770 reads per kilobase. Values are expressed as $\log_2$-fold change in the *LRPPRC*-KO cells compared
771 to the *LRPPRC* rescue cells. Mitoribosome profiling and RNA-seq data for *LRPPRC*-KO and
772 *LRPPRC*-reconstituted cell lines are deposited in GEO under the accession number GSE173283.
773 Mitoribosome profiling and RNA-seq data for the LSFC-reconstituted is deposited in GEO under
774 the accession number GSEXXXXXX.
775 The mitoRPF length distribution was determined from mitochondrial mRNA-aligned reads. First,
776 soft-clipped bases were removed using jvarkit [81], then frequency for each length was output
777 using Samtools stats [82].
778

779 **Data availability statement**

780 The atomic coordinates were deposited in the RCSB Protein Data Bank, and EM maps have been
781 deposited in the Electron Microscopy Data bank under accession numbers 8ANY and EMD-
782 15544.
783 The atomic coordinates that were used in this study: 6ZTJ (*E.coli* 70S-RNAP expressome
784 complex in NusG); 6ZTN (*E.coli* 70S-RNAP expressome complex in NusG); 1RKJ (human
785 Nucleolin); 5WWE (human hnRNPA2/B1); 1CVJ (Poly-adenylate binding protein, PABP)
786

787 **Additional References**

788 61. Aibara, S., Andréll, J., Singh, V. & Amunts, A. Rapid isolation of the mitoribosome from
789 Hek Cells. *Journal of Visualized Experiments* (2018). doi:10.3791/57877.
790 62. Zivanov, J. *et al.* New tools for automated high-resolution cryo-EM structure determination
791 in relion-3. *eLife* **7,** (2018).
792 63. Zivanov, J., Nakane, T. & Scheres, S. H. A bayesian approach to beam-induced motion
793 correction in Cryo-EM single-particle analysis. *IUCrJ* **6,** 5–17 (2019).
794 64. Zhang, K. GCTF: Real-time CTF determination and correction. *Journal of Structural*
795 *Biology* **193,** 1–12 (2016).
796 65. Zivanov, J., Nakane, T. & Scheres, S. H. Estimation of high-order aberrations and
797 anisotropic magnification from Cryo-EM data sets in *relion*-3.1. *IUCrJ* **7,** 253–267 (2020).
798 66. Emsley, P. & Cowtan, K. *Coot*: Model-building tools for Molecular Graphics. *Acta*
799 *Crystallographica Section D Biological Crystallography* **60,** 2126–2132 (2004).
800 67. Afonine, P. V. *et al.* Real-space refinement in*phenix*for cryo-EM and Crystallography. *Acta*
801 *Crystallographica Section D Structural Biology* **74,** 531–544 (2018).

802 68. Bourens, M., Boulet, A., Leary, S.C. & Barrientos, A. Human COX20 cooperates with
803 SCO1 and SCO2 to mature COX2 and promote the assembly of cytochrome *c* oxidase. *Hum.*
804 *Mol. Genet.* **23**, 2901-2913 (2014).
805 69. Fernandez-Vizarra, E. *et al.* Isolation of mitochondria for biogenetical studies: An update.
806 *Mitochondrion* **10**, 253-262 (2010).
807 70. Moreno-Lastres, D. *et al.* Mitochondrial Complex I Plays an Essential Role in Human
808 Respirasome Assembly. *Cell Metab.* **15**, 324-335 (2012).
809 71. Lowry, O.H., Rosebrough, N.J., Farr, A.L. & Randall, R.J. Protein measurement with the
810 Folin phenol reagent. *J. Biol. Chem.* **193**, 265-275 (1951).
811 72. Laemmli, U.K. Cleavage of structural proteins during the assembly of the head of
812 bacteriophage T4. *Nature* **227**, 680-685 (1970).
813 73. Diaz, F., Barrientos, A. & Fontanesi, F. Evaluation of the mitochondrial respiratory chain
814 and oxidative phosphorylation system using blue native gel electrophoresis. *Curr. Protoc.*
815 *Hum. Genet.* Chapter, Unit19.14. (2009).
816 74. Timón-Gómez, A. *et al.* Protocol for the analysis of yeast and human mitochondrial
817 respiratory chain complexes and supercomplexes by Blue Native-PAGE. *STAR Protocols* **1**,
818 100119 (2020).
819 75. Martin, M. Cutadapt removes adapter sequences from high-throughput sequencing reads.
820 *EMBnet J.* **17**, 10-12 (2021).
821 76. Kim, D., Paggi, J.M., Park, C., Bennett, C. & Salzberg, S.L. Graph-based genome alignment
822 and genotyping with HISAT2 and HISAT-genotype. *Nat. Biotechnol.* **37**, 907-915 (2019).
823 77. Pertea, M. *et al.* StringTie enables improved reconstruction of a transcriptome from RNA-
824 seq reads. *Nat. Biotechnol.* **33**, 290-295 (2015).
825 78. Frazee, A.C. *et al.* Ballgown bridges the gap between transcriptome assembly and
826 expression analysis. *Nat. Biotechnol.* **33**, 243-246 (2015).
827 79. Love, M.I., Huber, W. & Anders, S. Moderated estimation of fold change and dispersion for
828 RNA-seq data with DESeq2. *Genome Biol.* **15**, 550 (2014).
829 80. Liao, Y., Smyth, G.K. & Shi, W. The R package Rsubread is easier, faster, cheaper and
830 better for alignment and quantification of RNA sequencing reads. *Nucleic Acids Res.* **47**, e47
831 (2019).
832 81. Lindenbaum, P. & Redon, R. bioalcidae, samjs and vcffilterjs: object-oriented formatters
833 and filters for bioinformatics files. *Bioinformatics* **34**, 1224-1225 (2018).
834 82. Danecek, P. *et al.* Twelve years of SAMtools and BCFtools. *Gigascience* **10** (2021).
835

836 **Acknowledgments**

837 We thank S. Aibara and J. Andrell for help with data collection. The research was funded by the
838 Swedish Foundation for Strategic Research (FFL15:0325), Ragnar Söderberg Foundation
839 (M44/16), European Research Council (ERC-2018-StG-805230) , Knut and Alice Wallenberg
840 Foundation (2018.0080) , NIH R01 (R01-GM123002) to SC, NIH R35 (R35-GM118141) to AB.
841 V.S. was supported by the Horizon 2020 - Marie Sklodowska-Curie Innovative Training
842 Network (721757), Y.I. was supported by H2020-MSCA-IF-2017 (799399-Itohribo), and C.M
843 was supported by the Eunice Kennedy Shriver National Institute Of Child Health & Human

Development of the National Institutes of Health under Award Number F30HD107939. The SciLifeLab cryo-EM facility is funded by the Knut and Alice Wallenberg, Family Erling Persson, and Kempe foundations. The content is solely the responsibility of the authors and does not necessarily represent the official views of the National Institutes of Health.

Author contributions

V.S. collected cryo-EM data, processed the data, and built the models. V.S., Y.I. and A.A. performed structural analysis. C.M., F.F. and A.B. performed mitochondrial translation, OXPHOS, and RNAseq analysis. I.S., M.C. and S.C. performed mitoribosome profiling and RNAseq analysis. V.S., M.H. and A.A. performed evolutionary analysis. A.A. wrote the manuscript. All authors contributed to data interpretation and manuscript writing.

Competing Interests Statement

The authors declare no competing interests.

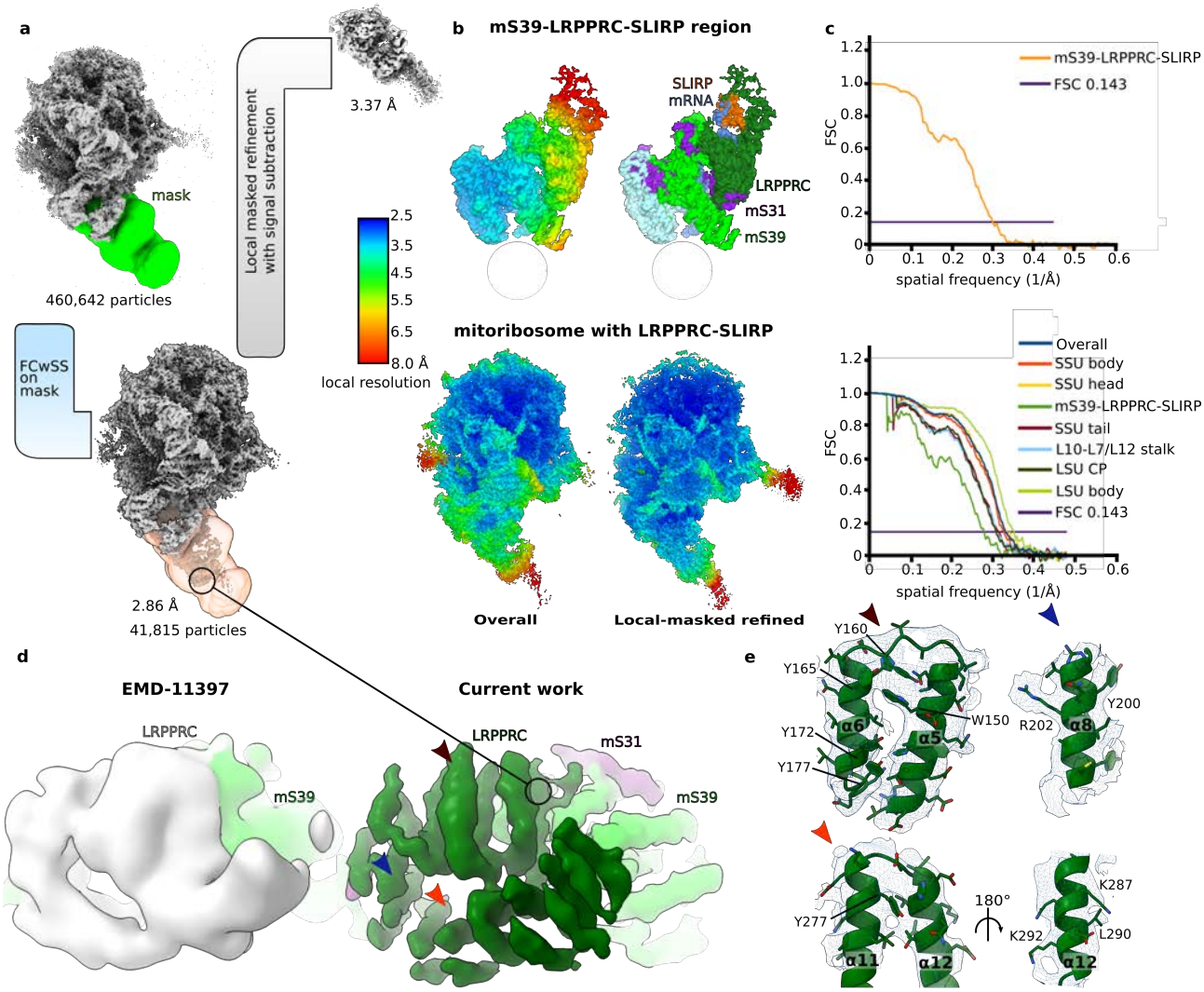

Extended Data Fig. 1. Cryo-EM data processing and map for mS39-LRPPRC-SLIRP region. **a.** Focused 3D-classification with signal subtraction using mask around mS39-LRPPRC-SLIRP region (transparent orange) of mitoribosome particles to identify LRPPRC-SLIRP containing monosome particles (2.86 Å overall resolution), followed by, masked refinement with signal subtraction on mS39-LRPPRC-SLIRP region to improve the local resolution. **b.** The mS39-LRPPRC-SLIRP map is shown colored by local resolution (top left) and by proteins assigned to the density (top right). The consensus map (bottom left) and the masked refined maps shown as a single composite map colored by local resolution (bottom right). **c.** Fourier shell correlation curves for the post-subtraction masked refined mS39-LRPPRC-SLIRP map (top) and individual masked refined maps. **d.** Map comparison for LRPPRC region between our work and EMD-11397. The map has been Gaussian filtered for better visibility. **e.** Density shown as mesh around helices α5-6, 8 and 11-12. Corresponding regions are indicated with arrows in panel (d).

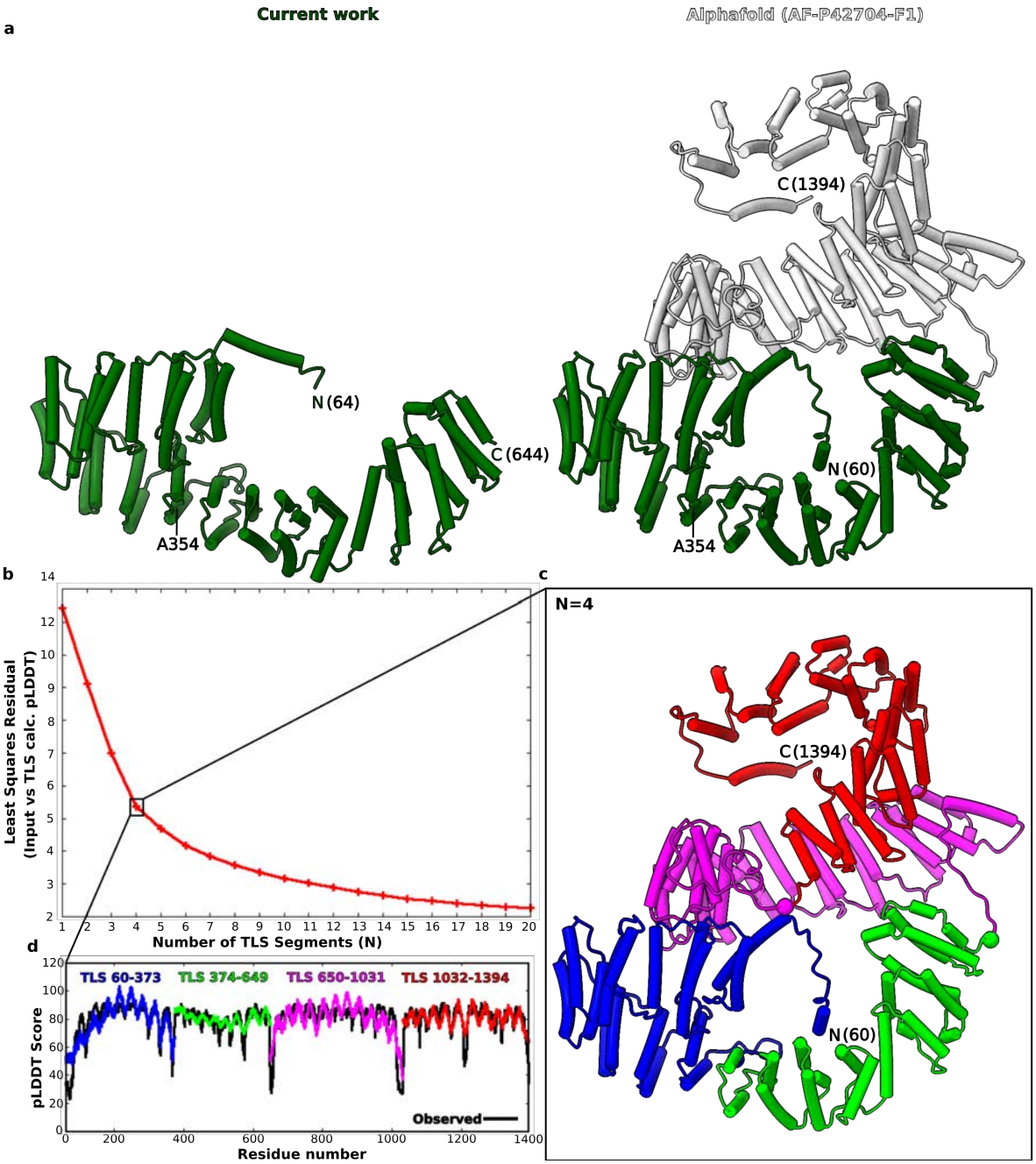

Extended Data Fig. 2. *AlphaFold* model and TLSMD analysis of LRPPRC.

a. The modeled region of LRPPRC (residues 64-644) is compared with the AlphaFold model (AF-P42704-F1) of full length (right). The modeled region is green, the unmodeled is white. The position of LSFC variant (A354V) is indicated. **b.** TLSMD analysis of the AlphaFold model of LRPPRC up to 20 TLS segments (N). Graph plots least-square residuals assigned per-residue confidence score values (pLDDT) versus those calculated by TLS analysis. **c.** Model colored by TLS segments for N=4. Regions between the segments with high pLDDT values correspond to loop regions and are shown as spheres **d.** Comparison of AlphaFold assigned versus calculated pLDDT values at N=4.

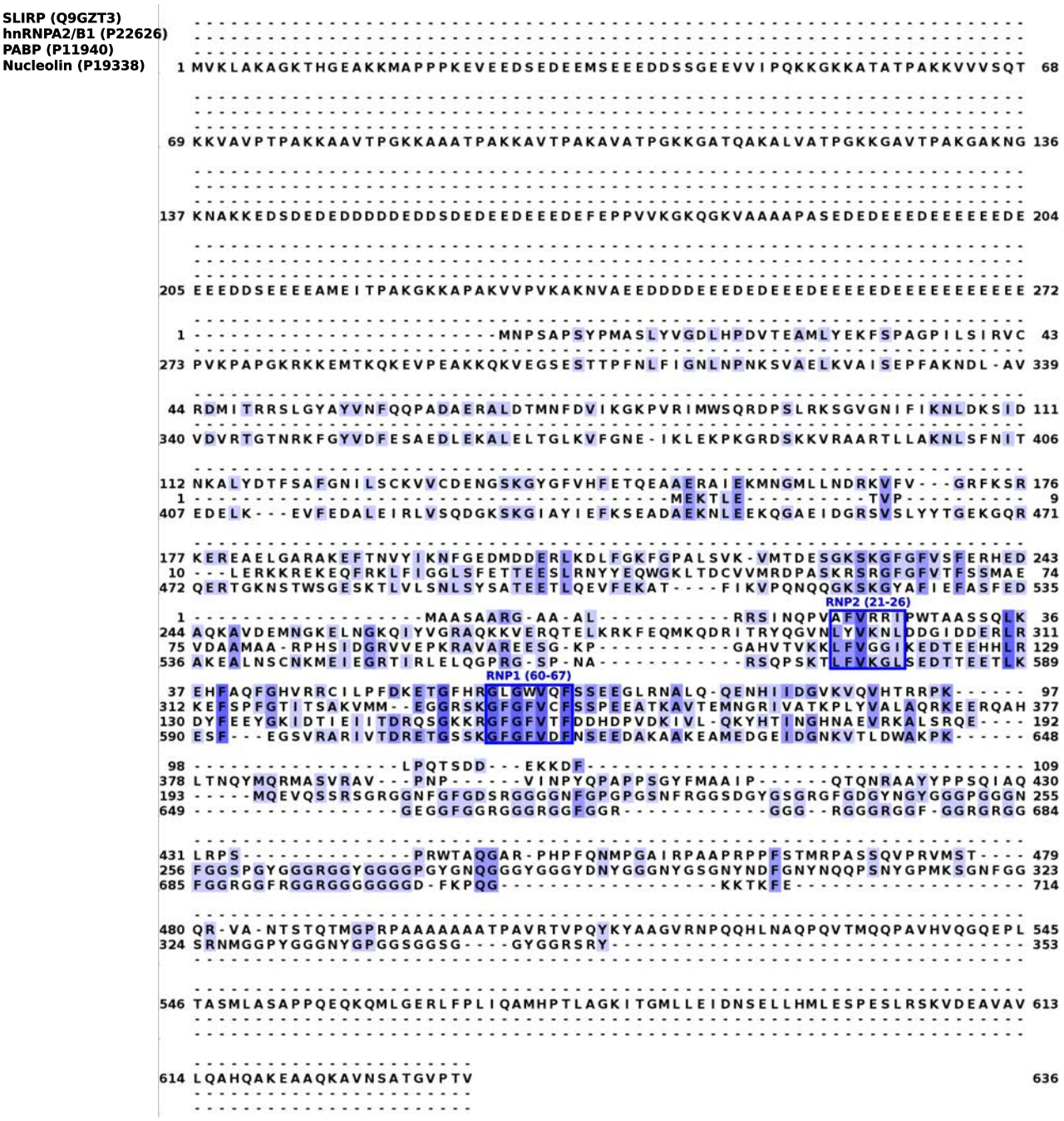

Extended Data Fig. 3. Multiple sequence alignment between SLIRP and representative RRM containing proteins. Alignment of SLIRP with representative RRM family proteins, heterogeneous nuclear ribnucleoproteins (hnRNPA2/B1), poly-A binding protein (PABP), and nucleolin shows conservation of submotifs RNP1 and RNP2 highlighted and indicated by corresponding residue numbers in SLIRP. Individual sequences are marked by residue numbers in the beginning and end and residues are colored by present identity.

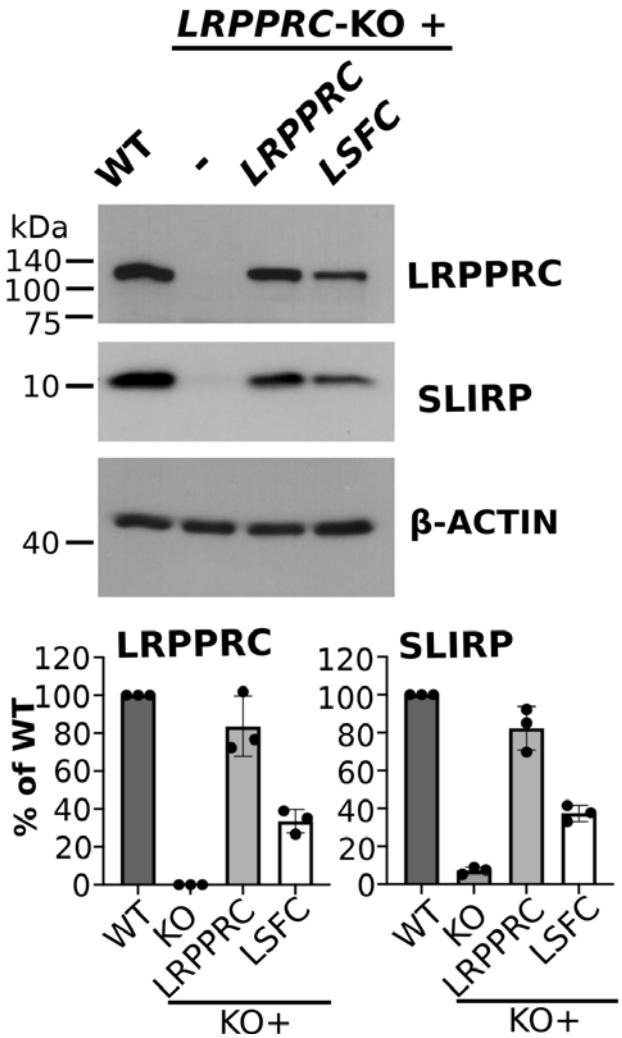

Extended Data Fig. 4. Reconstitution of the *LRPPRC*-KO with wild-type and LSCF variants of LRPPRC. Immunoblot analysis to estimate the steady-state levels of LRPPRC and SLIRP in the indicated cell lines. β-ACTIN was used as a loading control. The images were digitized, and the specific signals were quantified using the histogram function of Adobe Photoshop from three independent repetitions.

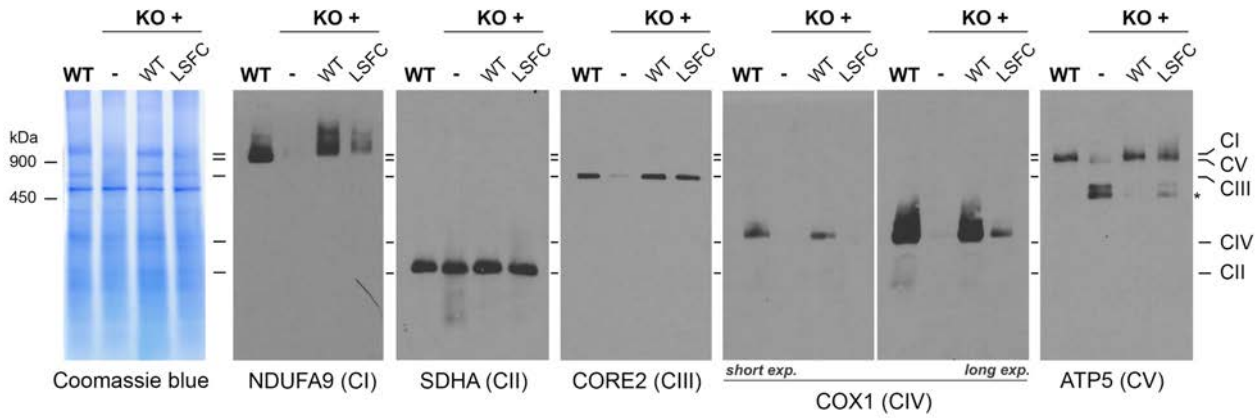

Extended Data Fig. 5. Mitochondrial protein synthesis is altered in *LRPPRC*-KO cells. Blue-native PAGE analyses in WT, *LRPPRC*-KO, and KO+WT cell lines. Intact respiratory complexes were extracted from purified mitochondria using 1% n-dodecyl β-D-maltoside. An asterisk indicates the ATPase **(**CV) F_1 module that accumulates due to the low levels of the mitochondrion-encoded F_O module subunits ATP6 and ATP8.

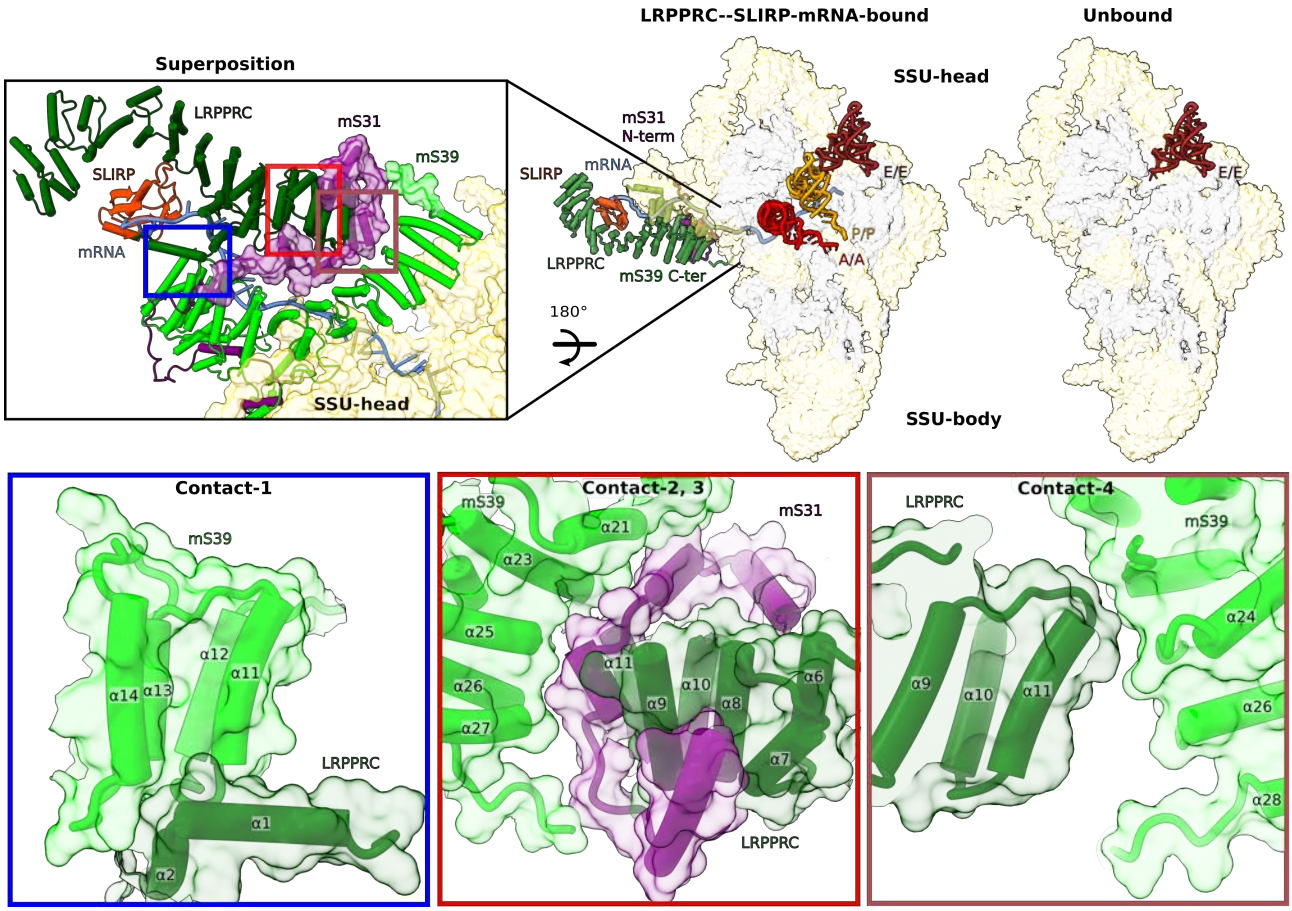

Extended Data Fig. 6. LRPPRC-SLIRP contacts with the SSU head. a. Comparison of SSU from mitoriboome:LRPPRC-SLIRP complex with SSU from E-site tRNA bound monosome. Zoom-in shows N-terminal region of mS31 and C-terminal loop of mS39 (in surface) stabilized by LRPPRC. **b.** Contact regions of LRPPRC with mS31 and mS39 shown in cartoon and surface representations.

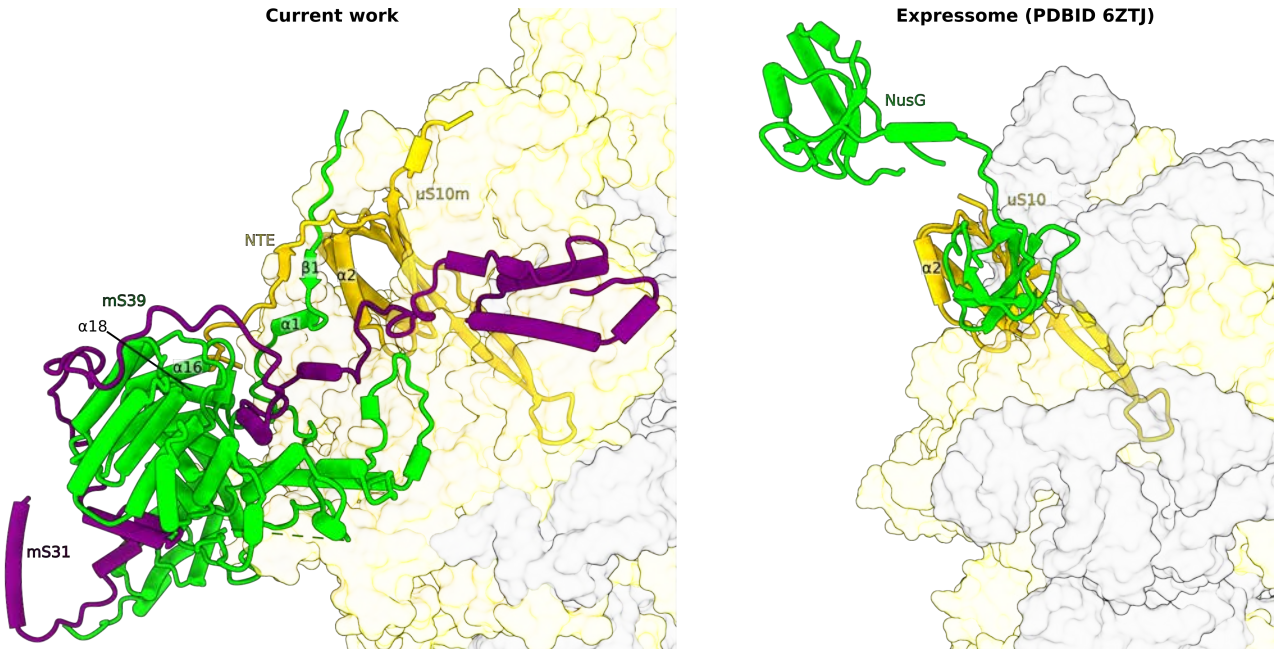

Extended Data Fig. 7. Close-up view of uS10m interactions with mS31-mS39.

Interface between uS10m with mS31-mS39 that serve as the platform for LRPPRC-SLIRP is similar to that formed between uS10 and NusG that binds RNA polymerase in bacterial expressome [8].

Structural basis of LRPPRC-SLIRP-dependent translation by the mitoribosome

Vivek Singh[1,7], J. Conor Moran[2,7], Yuzuru Itoh[1,6,*], Iliana C. Soto[3], Flavia Fontanesi[2], Mary Couvillion[3], Martijn A. Huynen[4], Stirling Churchman[3,*], Antoni Barrientos[5,*], Alexey Amunts[1,*]

[1] Science for Life Laboratory, Department of Biochemistry and Biophysics, Stockholm University, 17165 Solna, Sweden.

[2] Department of Biochemistry and Molecular Biology, University of Miami Miller School of Medicine, Miami, FL, 33136, USA

[3] Blavatnik Institute, Department of Genetics, Harvard Medical School, Boston, MA, 02115, USA.

[4] Centre for Molecular and Biomolecular Informatics, Radboud Institute for Molecular Life Sciences, Radboud University Medical Center, Nijmegen, the Netherlands.

[5] Department of Neurology, University of Miami Miller School of Medicine, Miami, FL, 33136, USA.

[6] Current position: Department of Biological Sciences, Graduate School of Science, The University of Tokyo, 113-0033 Tokyo, Japan.

[7] These authors contributed equally

* correspondence: yuzuru.itoh@bs.s.u-tokyo.ac.jp, churchman@genetics.med.harvard.edu, abarrientos@med.miami.edu, amunts@scilifelab.se

SUPPLEMENTARY INFORMATION

Table of contents:

Supplementary Table 1. Data collection and model statistics

SI Video 1. Structure of LRPPRC-SLIRP module bound to monosome

Supplementary table 1. Data collection and model statistics.

	Monosome with LRPPRC:SLIRP PDB: 8ANY EMD-15544
Data collection and processing	
Electron microscope	Titan Krios
Camera	K2 Summit (counting mode)
Magnification	165,000
Voltage (kV)	300
Electron exposure ($e^-/Å^2$)	29-32
No. of frames	20
Defocus range (μm)	-0.6 to -2.8
Pixel size (Å)	0.83
Symmetry imposed	C_1
Final particle number (no.)	41,815
Map resolution (Å) (Overall/ LSU-body/ CP/ L10-L12-stalk/ L1-stalk/ SSU-body/ SSU-head/ mS39/ SSU-tail/ mS39-LRPPRC-SLIRP)	2.85/2.69/ 3.07/ 3.07/ −/ 2.89/ 2.84/−/ 3.02/3.37
FSC threshold	0.143
Map resolution range (Å)	2.5-8.0
Refinement	
Initial model used (PDB code)	6ZSG, 6RW4
Model resolution (Å)	2.7
Model to map CC (CC_{volume})	0.84
FSC threshold	0.5
Map-sharpening *B* factor ($Å^2$) (Overall/ LSU-body/ CP/ L10-L12-stalk/ L1-stalk/ SSU-body/ SSU-head/ mS39/	-33/ -28/ -58/ -49/−/ -39/ -39/−/-55/ -60
Model composition	
Non-hydrogen atoms	356138
Hydrogen atoms	160529
Protein chains	90
RNA chains	7
Protein residues (non-modified/ *N*-acetylAla/ *N*-acetylSer/ *N*-acetylThr O^1-methylisoAsp)	15624/3/1/1/1
RNA residues (non-modified/ mG/ mU/ m^1A/ m^2G/ψ /m^4C/ m^5C/ m^5U/ $m^6{}_2A$)	2822/2/ 1/ 2/ 1/ 2/ 1/ 1/ 1/ 2
Ligands (ATP/ GDP/ NAD/ 2Fe-2S/ spermine/ spermidine/ putrescine)	1/ 1/ 1/ 3 /1 /4/ 1
Ions (Zn^{2+}/ K^+/ Mg^{2+})	3/ 49/ 206
Waters	6,926
Mean atomic *B*-factor ($Å^2$)	
Protein	38.28
RNA	36.42
Ligand	18.47
Water	15.21
Validation	
Ramanchandran plot (%)	
Outliers	0.05
Allowed	1.85
Favored	98.11
Clash score	2.64
RMSD	
Bonds (Å)	0.002
Angles (°)	0.432
Rotamer outliers (%)	0.00
C_β outliers (%)	0.00
CaBLAM outliers (%)	0.90

Supplementary Video 1. Structure of LRPPRC-SLIRP module bound to monosome.

The video shows the structure of LRPPRC-SLIRP determined in this work and how docking of mRNA on SSU is achieved by LRPPRC-SLIRP together with mito-specific proteins mS31 and mS39.